The Astrophysical Journal, 940:43 (20pp), 2022 November 20 https://doi.org/10.3847/1538-4357/ac98b3

Temporal Evolutions and Quasiperiodic Variations Present in the Sunspot Number and Group Sunspot Area Data Measured at Kodaikanal Observatory for Solar Cycles 14–24

Belur Ravindra[1], Partha Chowdhury[2], Pratap Chandra Ray[3], and Kumaravel Pichamani[1]
[1] Indian Institute of Astrophysics, Koramangala, Bengaluru-560034. India; ravindra@iiap.res.in
[2] University College of Science and Technology, Department of Chemical Technology, University of Calcutta, 92, A.P.C. Road, Kolkata, 700009, West Bengal, India
[3] Post Graduate Department of Mathematics, Bethune College, University of Calcutta, 700006 Kolkata, India
Received 2022 March 13; revised 2022 September 30; accepted 2022 October 6; published 2022 November 18

Abstract

The Kodaikanal Observatory has made synoptic observations of the Sun in white light since 1904, and these images are sketched on the Stonyhurst grids called Sun charts. These continuous hand-drawn data sets are used for long-term studies of the Sun. This article investigates temporal and periodic variations of the monthly hemispheric sunspot number and sunspot group area for 1905–2016, covering solar cycles 14–24. We find that the temporal variations of the sunspot number and group area are different in each hemisphere and peak at different times of the solar cycle in the opposite hemisphere. For both data sets, Cycle 19 shows maximum amplitude. For the sunspot number time series, Cycle 24 was the weakest, and Cycle 15 for the group area. The existence of double peaks and violation of the "odd–even rule" was found in both data sets. We have studied the periodic and quasiperiodic variations in both time series using the wavelet technique. We noticed that, along with the fundamental mode of the ∼11 yr cycle and polarity reversal period of 22 yr, the sunspot activity data also exhibited several midterm periodicities in the opposite hemispheres, in particular the Rieger-group, and quasi-biennial periodicities. The temporal evolution of these detected quasi-periodicities also differs in the northern and southern hemispheres. We analyzed the data set statistically to understand the bulk properties and coupling between the opposite hemispheres. The study indicates that the two hemispheric data sets differ, but some dependency could be present.

Unified Astronomy Thesaurus concepts: Sunspot number (1652); Sunspot cycle (1650); Sunspots (1653)

1. Introduction

The sunspots are the most prominent features visible even with a small-sized telescope from the Earth. The first record of these features started 400 yr ago. The sunspots number count began at the starting of the 18th century (Wolf 1861) with or without the sunspot drawings made on the charts. Later, the sunspot counts were refined with correction factors to accommodate all the observatory data taken with different-sized telescopes (Wolf 1851; Wolfer 1902). The refined sunspot number records were used to study various properties and characteristics of sunspots and activity cycle (Gleissberg 1939, 1940, 1943, 1944). In the late 19th century, several observatories in the world had measured the sunspot group area along with the sunspot number (e.g., Hoyt et al. 1983). Among them, the Greenwich data have the longest record of the sunspot number and sunspot group area (Hathaway 2015).

With the recorded sunspot number, it was noticed that sunspots have an 11 yr periodicity. On using several years of data, it was realized that the sunspot cycle ranges between 8.5 and 13.5 yr. At the beginning of the 19th century, the 11 yr periodicity was noted as the appearance and disappearance of sunspots on the Sun's disk. Later, in the 20th century, it was seen that this is also related to the reversal in the polarity of sunspot groups. It was also seen that, over the 11 yr, the polar field was observed to be out of phase with the solar cycle (Babcock 1959). In addition to the 11 yr cycle, a shorter period such as a 27 day periodicity was also noticed. This time interval is attributed to the rotation period of the low-latitude sunspots on the Sun.

During the later part of the 20th century, a 154 day periodicity was observed in the flare data (Rieger et al. 1984), sunspot number, and area data as well (Lean & Brueckner 1989; Carbonell & Ballester 1990). Several midrange periodicities were observed between the 27 day and 11 yr periods. Those are referred to as quasi or midrange periodicities (e.g., Bai 2003; Chowdhury et al. 2009; Kudela et al. 2010, and the references therein). The Rieger-type periodicity and midrange periodicities were observed in the hemispheric sunspot area (Lean 1990) and plage area (Chowdhury et al. 2022). However, it was reported only in a few cycles of hemispheric sunspot number data (Temmer et al. 2006).

The hemispheric sunspot number data extracted from the Kanzelhöhe Solar Observatory (KSO), Austria are available from 1975 to 2000 (Temmer et al. 2002). By combining the KSO data with the Skalnaté Pleso Observatory, Slovak Republic sunspot data, Temmer et al. (2006) made the sunspot number data starting from 1945 until 2004. They have normalized the data with the International sunspot Number full sphere sunspot number data and then compared it with the sunspot Index Data Center (SIDC) hemispheric sunspot number data, which started in 1992 and continues until today. These data have reported the north–south asymmetry in the hemispheric sunspot number and rotational period in both hemispheres. Recently, Veronig et al. (2021) have extended this time series and made the hemispheric sunspot number catalog starting from 1874 until 2020 and studied some of the hemispheric properties of solar activity.

At the Kodaikanal observatory, the sunspot observations started in 1905 using photographic plates and continue to use photographic films. The photographic record of white-light

images is digitized at the Kodaikanal Observatory (KO; Ravindra et al. 2013; Mandal et al. 2017). Along with the photographs, sunspots, plages, and filament drawings are also made on the Stonyhurst grid by projecting the recorded image onto the paper. The hemispheric sunspot number and area parameters were extracted from these data sets (Ravindra et al. 2020). These data sets are useful for studying the sunspot cycles' different characteristic properties and midrange periodicities.

This paper presents the results on the temporal evolution of different solar cycles, coupling between the opposite hemispheres (statistical relationship), and midrange periodicities in the hemispheric sunspot number and area data extracted from the KO sunspot drawings. In Section 2, we present the data and the analysis procedure. Section 3 presents results on the quasi-biennial oscillations in the hemispheric sunspot parameters. Section 4 outlines the model fitting and their statistical accuracy. Section 5 delineates the nonlinear, statistical relationship between the northern and southern hemispheric sunspot numbers and group sunspot area time series. Section 6 summarizes the results, compares the asymmetry behavior, and quasi-biennial oscillations found in the sunspot number and area data. In the present work, we have utilized a number of analysis techniques, including the complex nonlinear wavelet method, autoregressive integrated moving average model (ARIMA) fitting with goodness of fit, and wavestrapping and dynamic time warping, to study the temporal variation and the statistical relationship between the long-term northern and southern hemispheric sunspot activities. We also compare them with past observations.

2. Data

Systematic observations of sunspots have been carried out at KO since 1904 with an unchanged single white-light telescope having a 10 cm objective (Sivaraman et al. 1993). Since 1976 January, these photographic plates were replaced by high-contrast films of size 25.4 cm × 30.5 cm. These photographic plates and the films have been recently digitized with the help of modern digitizer (see Ravindra et al. 2013, for details). Utilizing this century-long data set, several researchers investigated various aspects of the sunspots and their solar cycle characteristics (e.g., Mandal et al. 2017; Ravindra et al. 2021).

Along with this process, in parallel, drawings of the different observed features on the solar surface like sunspots, plages, and filaments were made on the Stonyhurst grids, which are called Sun charts. All those abovementioned solar magnetic indices were detected distinctly and optically marked with different colors in these Sun charts. This was furnished by projecting the sunspot images onto the Stonyhurst latitude and longitude grid with a binning of 5° in both directions. Thus, KO provides a repository of more than 100 yr of handwritten sunspot drawings covering nearly 10 solar cycles. These sunspot drawings are preserved for scientific studies with due care at the KO library. The information of daily solar observations as well as the sky conditions were regularly maintained in a logbook. These drawings currently stand among one of the biggest and historical sunspot archives. Recently, Ravindra et al. (2020) have provided a detailed description about the Sun charts, the process of counting sunspot numbers, and determining the sunspot area from these historical grids.

Ravindra et al. (2020) determined the monthly average time series of sunspot numbers measured in both the opposite hemispheres using these KO Sun charts from 1905 January to 2016 November. The KO sunspot numbers are defined in the usual way as $R_n = k(10.g + n)$, where g and n are the number of sunspot groups and the total number of individual sunspots observed on the visible solar disk, respectively. The correction factor k is considered as 1.

From these Sun charts, the monthly mean time series of group sunspot areas of both the northern and southern hemispheres were also extracted for the aforesaid time span. The sunspot group area represents the total area covered on the solar disk by all sunspots. A larger sunspot group implies areas of larger magnetic flux, which in turn indicates larger magnetic energy content of an active region. Coupled with magnetic complexity, it would give a measure of flare productivity of the group. Here, the sunspot group area measured on the solar disk is defined as: $A_M = 2A_s 10^6/\pi D^2 \cos(\rho)$. Here A_s is the measured size of a sunspot group, ρ is the angular distance of the center of the sunspot group to the center of the solar disk, and D is the diameter of the solar image. The unit of the sunspot group area is the millionth of the solar hemisphere (μHem), and the foreshortening effect has been corrected.

Figure 1 represent typical images of these KO Sun charts in which the sunspots, plages, and filaments are drawn to their size. Each of these features is shown in different colors. The area covered by the sunspots and plages is displayed next to those features and expressed in millimeters. These numbers are converted into millionth of hemisphere using the tables available at KO. The Kodaikanal active region number (KKL number) is shown next to the sunspot group region in pencil.

We have utilized the wavelet analysis tool (Torrence & Compo 1998) to study the periodic and quasiperiodic variations in the monthly averaged sunspot number and group area time series for the period 1905–2016, covering solar cycles 14–24. The wavelet analysis is a valuable tool that can reveal the presence of localized oscillations in the two-dimensional time-frequency domains. This method provides information about the exact location of the detected periods and their temporal variations present in a time series. To study the periodic behavior of the KO sunspot number and group sunspot area, we have used complex Morlet wavelet (Morlet et al. 1982) function,

$$\psi_n(\eta) = \pi^{-1/4} e^{i\omega_0 \eta} e^{-\eta^2}/2. \quad (1)$$

Here, ω_0 is a nondimensional frequency, and we have adopted $\omega_0 = 12$ as the midterm frequency (low periodic zone; 4 months–1.4 yr) range and $\omega_0 = 6$ for the low-frequency regime (long periods, 1.4–11 yr; Chowdhury et al. 2019; Ravindra et al. 2021). In addition to this, we have also investigated the presence of ~22 yr Hale cycle, which indicates the returning of the Sun's magnetic field in all the data sets considering $\omega_0 = 6$. The cone of influence (COI), which indicates a reduction in the wavelet power due to edge effects (Torrence & Compo 1998; Grinsted et al. 2004), is shown with a bold dashed line. In all wavelet spectra, the thin black contours represent the periods above the 95% confidence level considering the red-noise background and detected using the recipe by Grinsted et al. (2004).

Under the condition of the red-noise background, the discrete Fourier power spectrum, after normalization, takes the

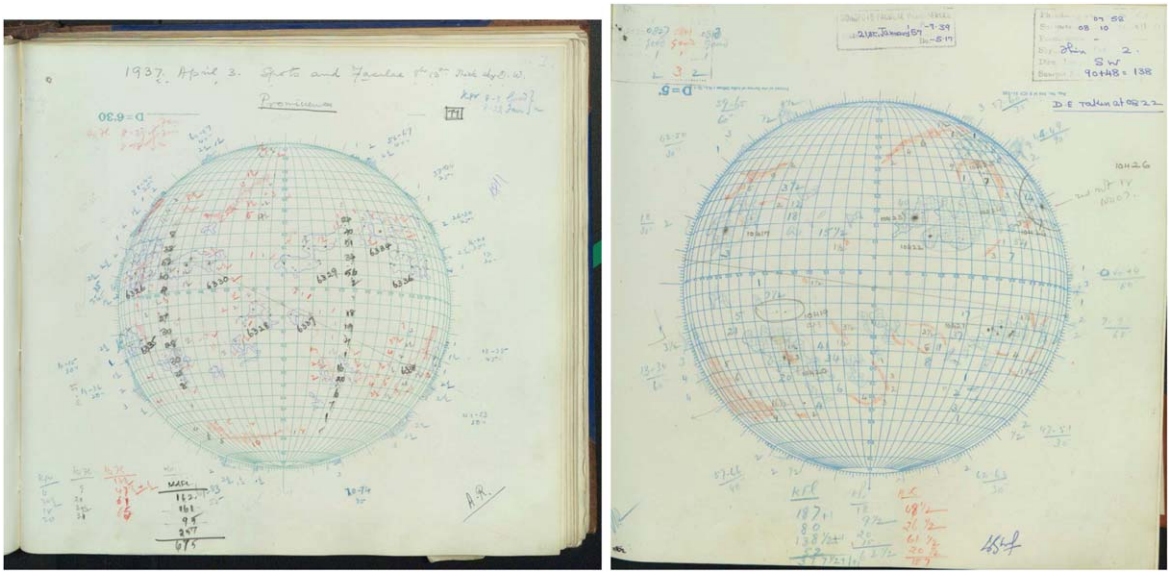

Figure 1. The sketches of sunspots, plages, filaments, and prominences are made on the Stonyhurst grid for two different days of observations. Specific colors are used to draw different features. The left-side image is for the date 1937 April 3, and the right side image is for the date 1957 January 21. The B_0 angle and p angle are shown the chart.

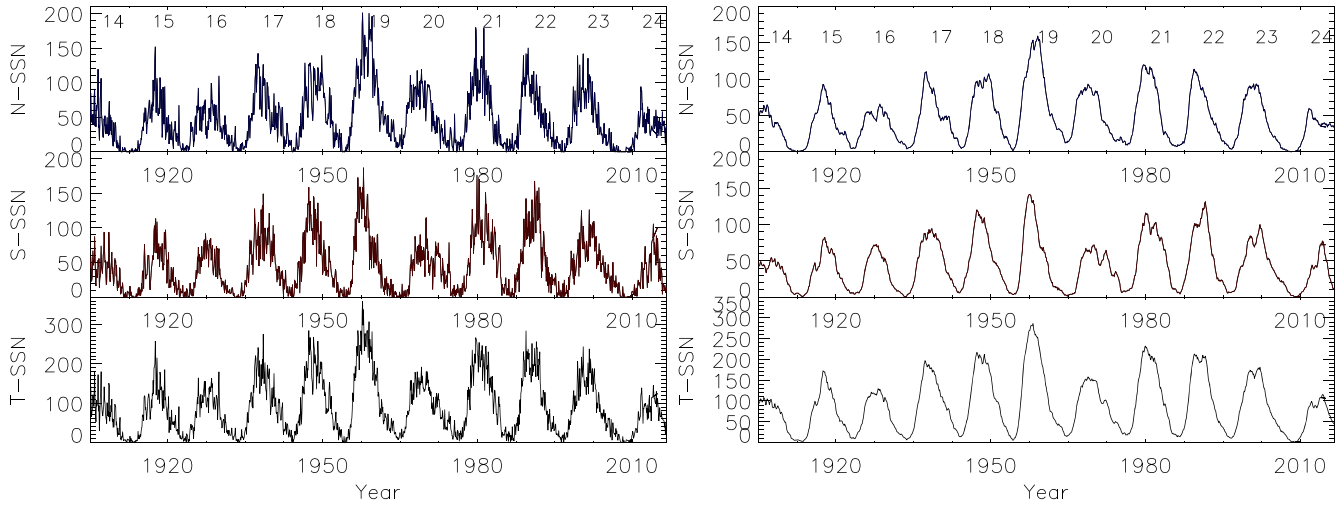

Figure 2. Left: Monthly average values of northern (top), southern (middle), and full-disk (bottom) sunspot numbers measured at KO from 1905 to 2016. Right: Same as the left-side plot but for the 13th month smoothed data.

form,

$$P_k = \frac{1-\alpha^2}{1+\alpha^2-2\alpha\cos(2\pi k/N)}, \quad (2)$$

where $k = 0, ..., N/2$ is the frequency index, N is the number of data points in the time series, and α is the lag-1 serial correlation coefficient. We have considered a red-noise background and the lag-1 serial correlation coefficients of all the data sets of KO sunspot number and group area under study.

The global wavelet power spectra (GWPS), which determine the wavelet power at each period and are averaged over the time span, have been calculated for all data sets under investigation considering red-noise background. The GWPS are formulated as,

$$\bar{W}^2(s) = \frac{1}{N}\sum_{n=0}^{N-1} |W_n(s)|^2. \quad (3)$$

Here $W_n(s)$ is the wavelet power, and N is the number of local wavelet spectra. In this way, we can detect an unbiased and consistent estimation of the true power spectrum of any time series. The working nature of these GWPS has similarities with the computation of the Fourier power spectra of the time series. Here, the GWPS plots with 95% confidence level have been calculated using the method provided by Torrence & Compo (1998).

3. Analysis and Results

3.1. Temporal Variations of Sunspot Numbers

Figure 2 (left) shows the monthly averaged sunspot numbers of both hemispheres and the whole solar disk for cycles 14–24 measured at the KO. The 13 months smoothed data sets are displayed in Figure 2 (right). These figures indicate that the sunspot number time series in both hemispheres and the whole disk follow a regular cyclic pattern of about 11 yr, with

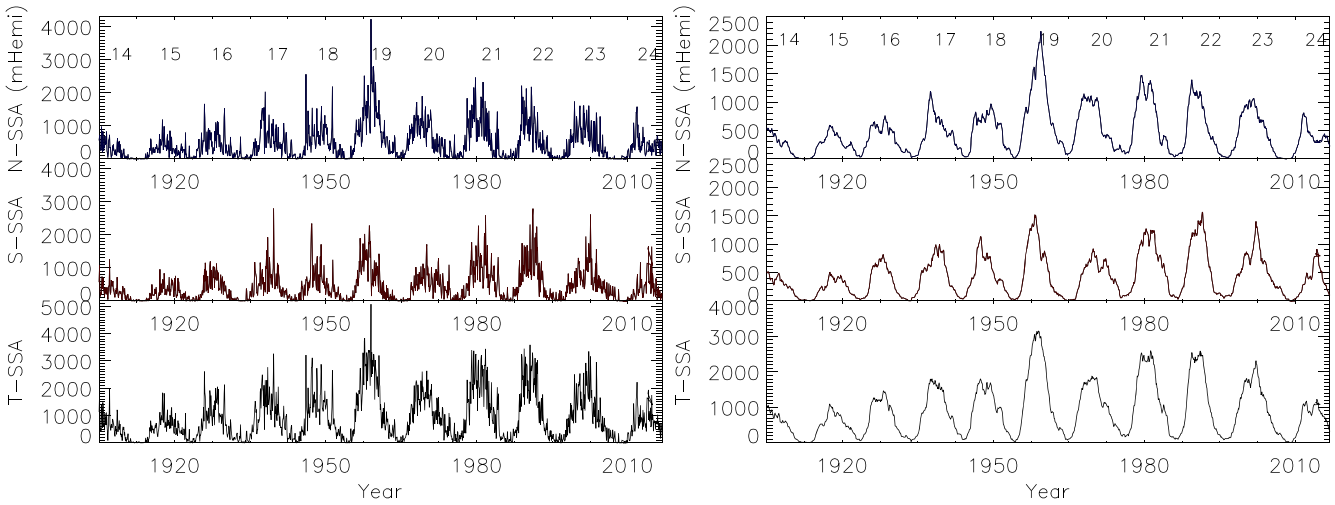

Figure 3. Left: Monthly average values of northern (top), southern (middle), and full-disk (bottom) sunspot group area (μHem) measured at KO from 1905 to 2016. Right: Same as the left-side plot but for the 13th month smoothed data.

different dynamical behavior in different sunspot cycles. Solar cycle 19 exhibits the maximum amplitude in all data sets. However, cycle 21 had the second-highest amplitude for the northern hemisphere and full-disk data. On the other hand, cycle 22 was the next powerful cycle for the southern hemisphere. Cycles 16, 20, and 24 are the weakest cycles for the northern, southern, and full-disk data. The strength of cycle 24 is distinctively weaker than cycles 23 and 22 in all cases.

Figure 2 (right) demonstrates that the even-numbered solar cycles have a low amplitude compared to the following odd-numbered solar cycles in the north, south and full-disk data. For example, cycles 16, 18, and 20 have smaller amplitude compared to the following odd-numbered cycles 17, 19, and 21. These behaviors satisfy the even–odd pair or G-O rule (Gnevyshev & Ohl 1948; Javaraiah 2012). However, we have noticed that the even-numbered cycle 22 has larger amplitude than the following cycle 23 in the northern, southern, and full-disk time series. So, the cycle 22–23 pair did not maintain the G-O rule. Utilizing the yearly group sunspot number and yearly sunspot numbers, Zolotova & Ponyavin (2015) showed that solar cycles 16–17 and 18–19 followed the even–odd pair rule instead of the odd–even rule. However, the concrete reason behind the pairing of adjacent cycles in a manner of even–odd or odd–even is still unknown (Hathaway 2015).

Several solar cycles exhibit double peaks during their maximum phase. In Figure 2 (right), we find that for cycles 16, 18, 21, 22, and 23, there are clear signatures of double peaks in both hemispheres and in the whole disk. For solar cycles 20 and 24, there is the signature of double peaks in the southern hemisphere and full-disk data. Cycle 20 shows multiple peaks and a step-like decrease during its descending phase, which is much more prominent in the case of the southern hemisphere. A step-like decrease is also detected only in the northern hemisphere during cycle 17. The amplitude of the sunspot number in the full disk shows a continuous decline from cycle 21 to 24. Recently, Veronig et al. (2021) constructed sunspot number time series for both hemispheres from 1874 to 2020 considering the WDC-SILSO sunspot number database and the Greenwich Royal Observatory sunspot area database, and the properties mentioned above detected in the KO sunspot number are also observed in their data set. There is quite a similarity about the strength and temporal evolution of sunspot numbers in the opposite hemispheres as well as the whole disk between these two databases during different cycles (see Figure 7 of Veronig et al. 2021).

3.2. Temporal Variations in the Sunspot Group Area

Figure 3 (left) shows the monthly averaged sunspot group area of the northern and southern hemispheres and the whole solar disk for cycles 14–24 measured at the KO. The monthly averaged and the 13th month data sets are displayed in Figure 3 (right). These figures indicate that the sunspot number and sunspot group area exhibit a cyclic pattern of about 11 yr. Solar cycle 19 shows the maximum amplitude and cycle 15 the weakest in all data sets. However, for full-disk data, the amplitude of cycle 24 is very close to that of cycle 15. Cycles 21 and 22 possess the second-highest amplitude for the northern and southern hemispheres. Both these cycles exhibit nearly the same amplitude in the full-disk data set.

Cycle 16 had the second weakest strength in the last century after cycle 15. The northern and southern hemisphere and full-disk data show that the pairs of cycles 16–17, 18–19, and 20–21 followed the G-O rule. The pair of cycles 22–23 violated the G-O rule in both the hemispheres and the full-disk data. The double peaks around the maximum epoch were prominent for cycles 16, 18, 21, 22, and 24. The existence of double peaks in the sunspot number and area in opposite hemispheres suggests that the origin is related to the presence of a subphotospheric dynamo. The descending phases of cycles 17, 18, and 20 exhibit multiple peaks and step-like complex patterns. From cycle 22 to 24, the peak height of the sunspot group area decreased continuously.

3.3. Periodicities in the KO Sunspot Number

The results of employing Morlet wavelet analysis to the monthly sunspot number of the northern and southern hemisphere as well as the whole solar disk are displayed in Figures 4, 5, and 6, respectively. Here, we focused on the midterm periodic and quasiperiodic variations in the monthly sunspot number for solar cycles 14–24.

Figure 4 (top left) represents the short periods present in the northern hemispheric sunspot number in the local wavelet spectrum. This figure indicates the presence of Rieger and

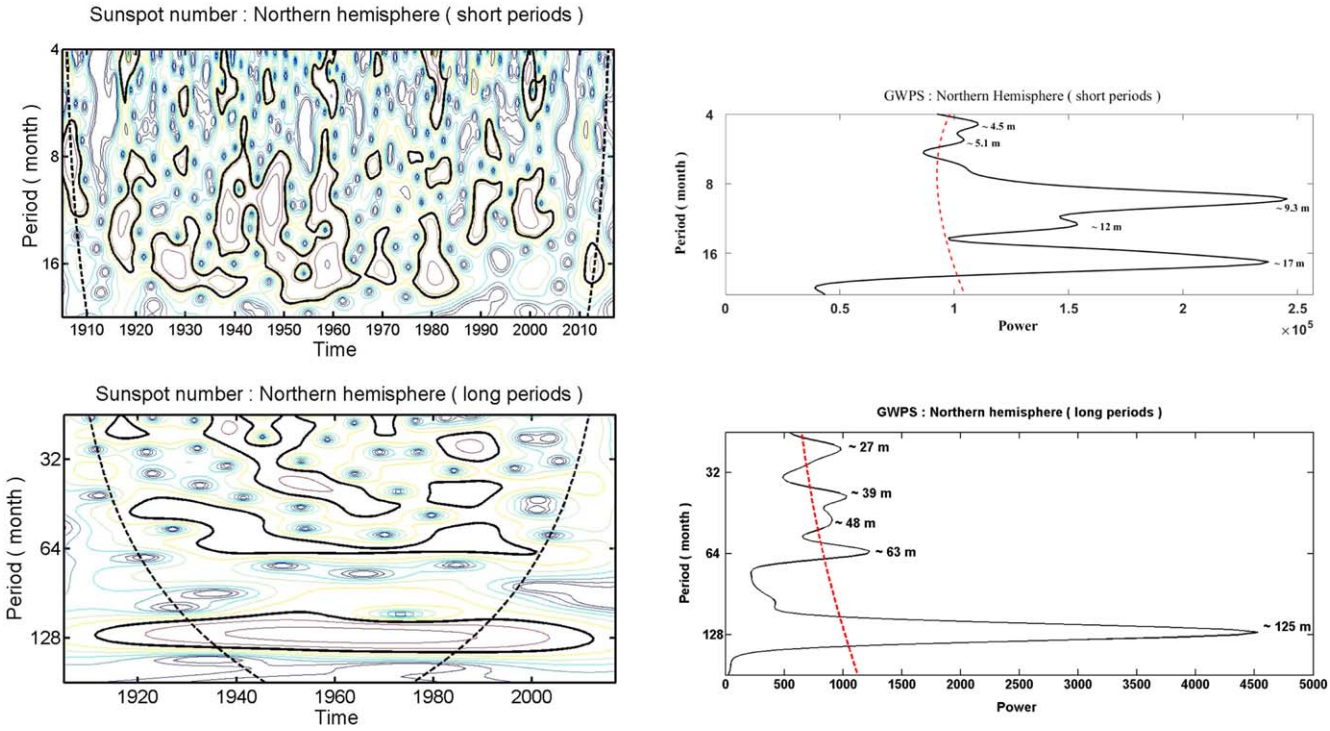

Figure 4. (a) Morlet wavelet spectra of the monthly KO sunspot number time series in the northern hemisphere. (b) Global power spectra for short-term periods mainly to study the Rieger-group periodicities. (c) Local Morlet wavelet power spectra to investigate the dynamical behaviors of QBOs (1.4–4 yr) and other long-term periods including the solar cycle period. (d) Similar to panel (b) for other long-term periods including the Schwabe cycle. The dotted lines in all global wavelet power spectra represent the 95% confidence level.

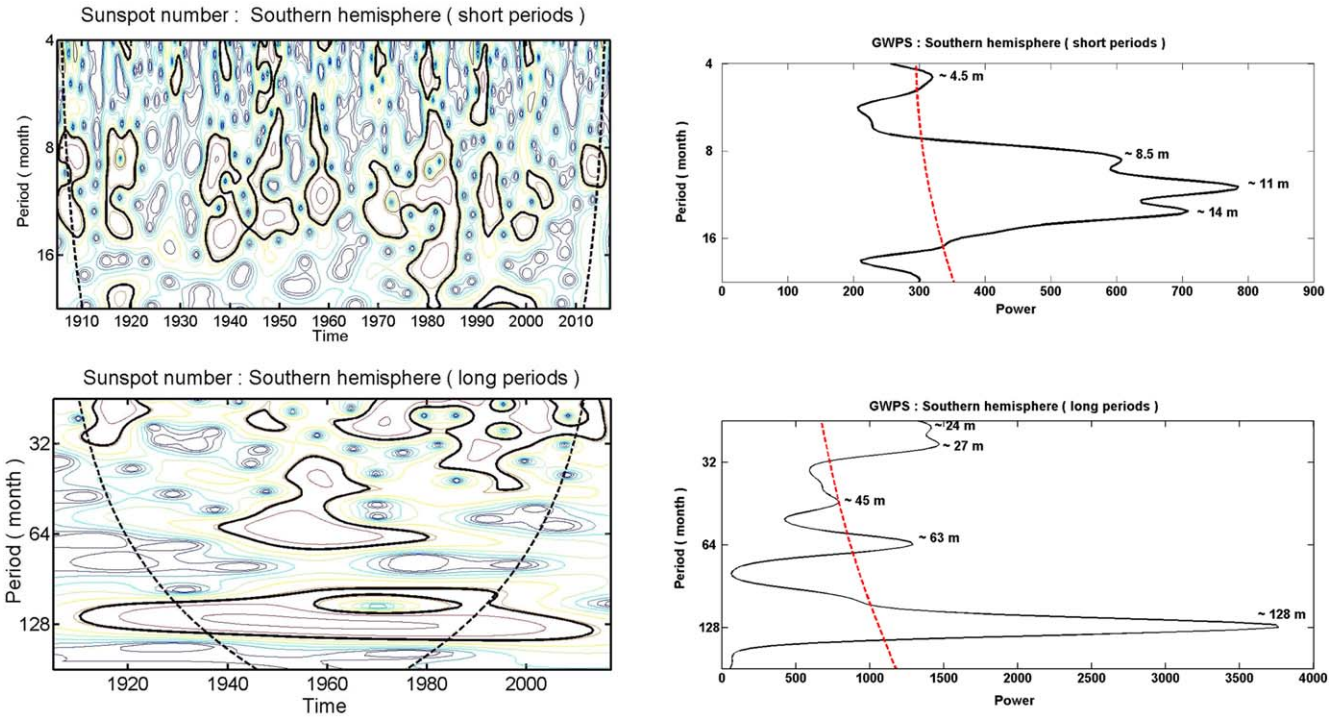

Figure 5. Same as Figure 4, but for the southern hemisphere.

Rieger-type periods in different solar cycles like 15, 17, 19, 21, and 23. The length of these groups of periods changes from 4 to 6 months. Quasi-periodicities of varying length between 300 and 365 days were clustered mainly in cycles 14, 15, 17 and 20, 22, and 23. The QBOs in the range of 1.2–1.4 yr were found during cycles 16–18 and also from the maximum phase of cycle 18 to the end of cycle 20 and partly in cycle 21.

Rieger-group oscillations were detected in different parts of cycles 16–23 in the southern hemisphere (Figure 5, top left). Intermediate-term periods in the range of 6–14 months were

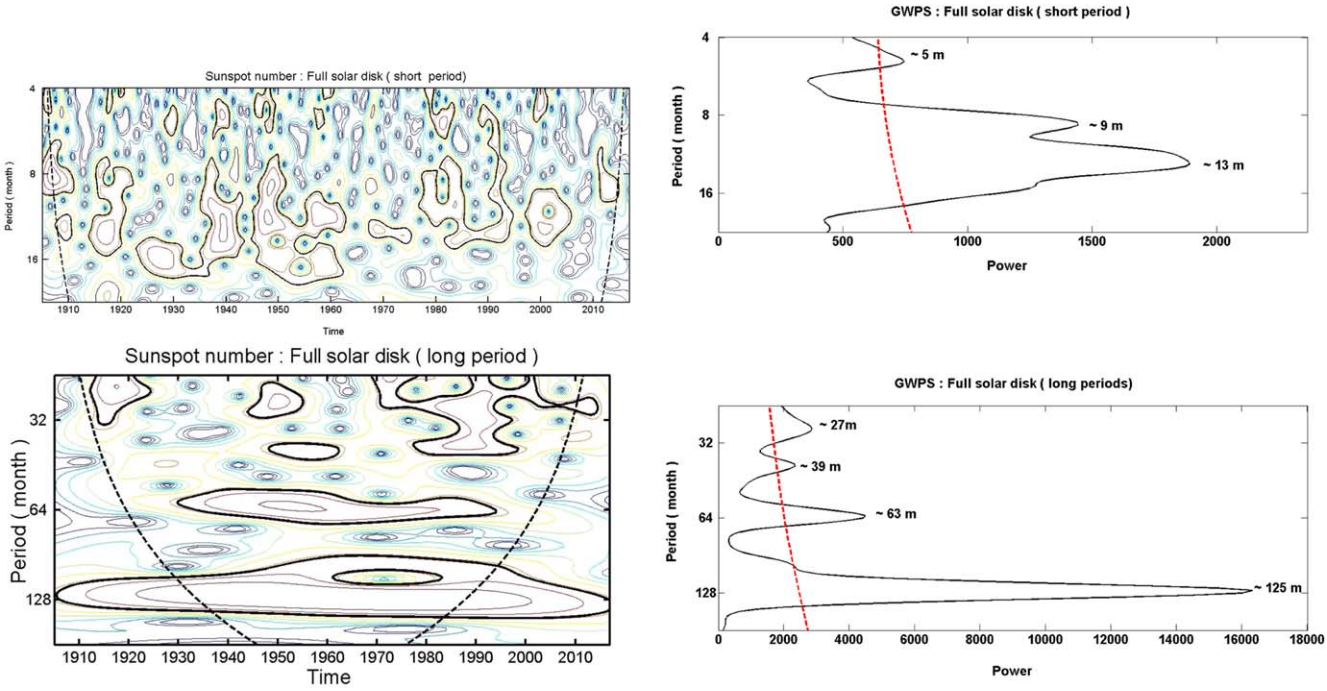

Figure 6. Same as Figure 4, but for the whole-disk data.

seen in cycle 15, cycles 17 to 20, and the descending phase of cycle 20 to the end of cycle 22 and 23.

Rieger-type periods were present in the data of the whole solar disk in scattered form during parts of cycles 16, 17, 18, 21, 22, and 23 (Figure 6, top left). Intermediate-term periods in the range of 7 months to 1 yr were detected in solar cycles, 14, 17, 18, 19, 21, 22, 23, and 24. QBOs in the range of 1.2–1.4 yr were concentrated in cycles 16–19 and cycle 23.

Figure 4 (bottom left) indicates that long-term QBOs in the range of 2–3.5 yr were present during cycles 17 to 20, cycle 22, and cycle 23 in the northern hemisphere. On the other hand, these periods were significant, mainly during cycles 19–24 in the southern hemisphere (Figure 5, bottom left). These QBOs were detected in cycles 14, 15, 17, and 20–24 in the sunspot number of the whole-disk data (Figure 6, bottom left). A long contour of a period of ∼5 yr appeared during cycles 15–23 in the northern hemisphere but persisted from the descending phase of cycle 17 and until the ascending phase of cycle 21 in the southern hemisphere. However, this period is significant during cycles 16–22 for the full solar disk. These three data sets exhibit a strong appearance of the ∼11 yr sunspot cycle period.

Figures 4 (top right and bottom right), 5 (top right and bottom right), and 6 (top right and bottom right) represent the GWPS of the corresponding local wavelet plots of the north, south, and total-disk data where the peaks of the significant periods are marked.

Table 1 shows that GWPS plots have statistically significant periods, which are also significant in the local wavelet plots. In particular, Rieger-type periods, QBOs, ∼5 yr, and solar cycle periodicity are prominent in the GWPS plots. Along with the most prominent ∼11 yr sunspot cycle, sunspots also exhibit a ∼22 yr cycle, which is known as the Hale cycle. Near the maximum epoch of the sunspot cycle, the Sun's polar magnetic field flips and returns to its original state after completing two solar cycles, and hence the length of this Hale cycle/Hale polarity law is ∼22 yr. It is commonly assumed that this Hale

Table 1
Periods Determined using the GWPS Applied to the KO sunspot Number Data for Cycles 14–24

Sunspot Number Data	Major Periods in Months (>95% Confidence Level)
Northern Hemisphere	∼5, ∼11, ∼17, ∼27, ∼39, ∼48, ∼63, ∼125
Southern Hemisphere	∼4.5, ∼8.5, ∼11, ∼14, ∼24, ∼27, ∼45, ∼63, ∼128
Whole Solar Disk	∼5, ∼9, ∼13, ∼27, ∼39, ∼63, ∼125

cycle is governed by the 22 yr magnetic dynamo cycle in the presence of the Sun's remnant magnetic field (Mursula et al. 2002; Hazra & Nandy 2019). Previously, a few studies indicated that the ∼22 yr Hale cycle is related with some atmospheric phenomena like air circumfluence oscillation, variations in the air pressure, and air temperature (Qu et al. 2012, and references therein). However, in the power spectrum analysis this cyclic nature is suppressed due to the presence of the very prominent ∼11 yr solar cycle period. We have studied the nature and variations in this magnetic cycle in the KO sunspot number data sets using the wavelet technique with $\omega_0 = 6$ (after reducing the power of the Schwabe cycle by applying the moving average method). Figure 7 shows the required plots in this context. From the GWPS plots it is found that the length of the Hale cycle is slightly higher in the northern hemisphere than in the southern one.

3.4. Periodicities in the KO sunspot Group Area

Figures 8, 9, and 10 show the results of the periodic variations in the KO monthly sunspot group area data after the Morlet wavelet analysis.

In the northern hemisphere, Rieger and Rieger-type of periods are present mainly during different phases of cycles 17, 18, 19, 21, 22, and 23 (Figure 8, top left). The QBOs in the range of 1.2–1.5 yr were strongly pronounced continually from cycles 16 to 21 and during cycle 24. Rieger-type periods were found in the southern hemisphere during cycles 17, 18, 19, 21,

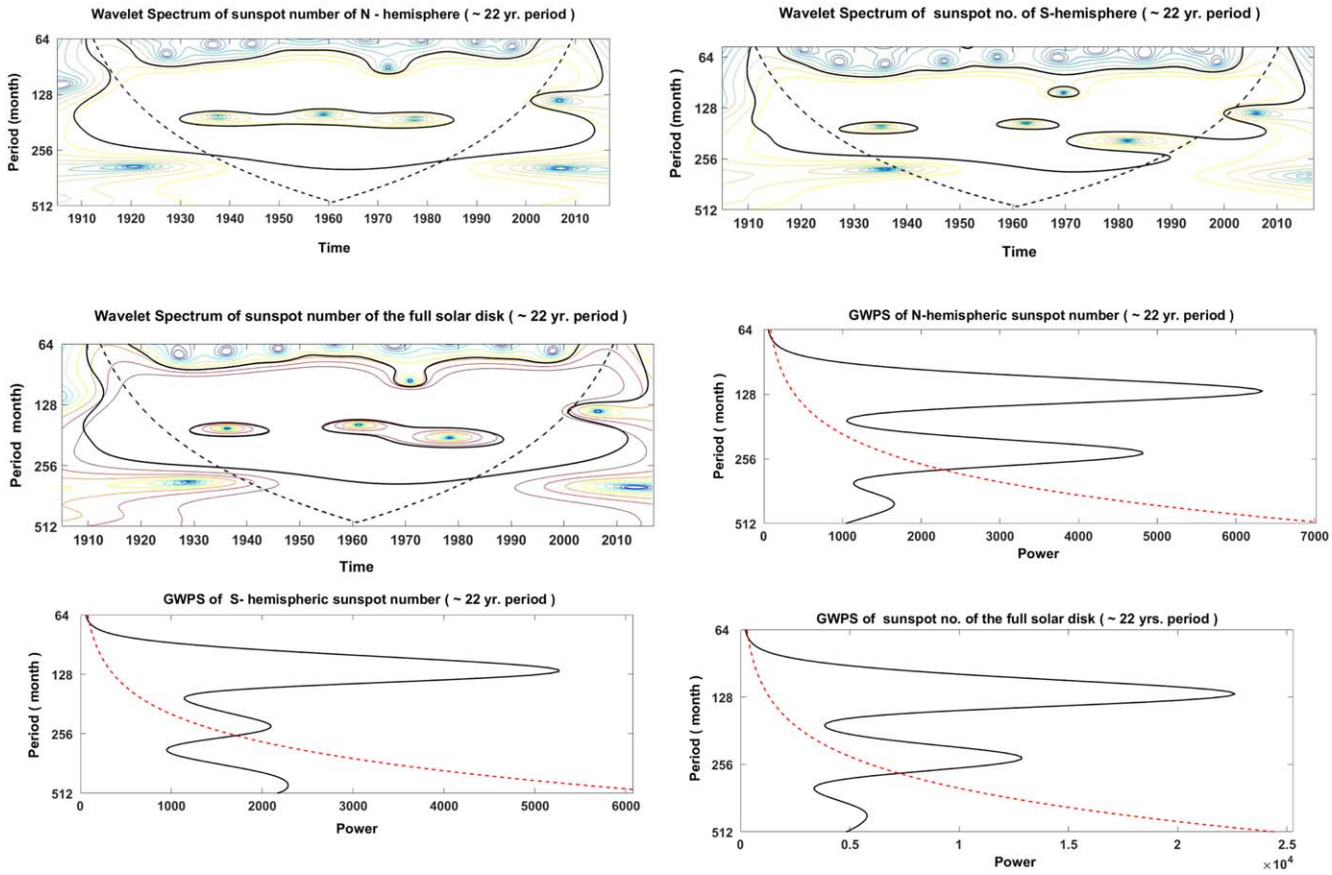

Figure 7. Wavelet plots showing the presence of the ∼22 yr Hale cycle in the hemispheric and full-disk sunspot number data sets.

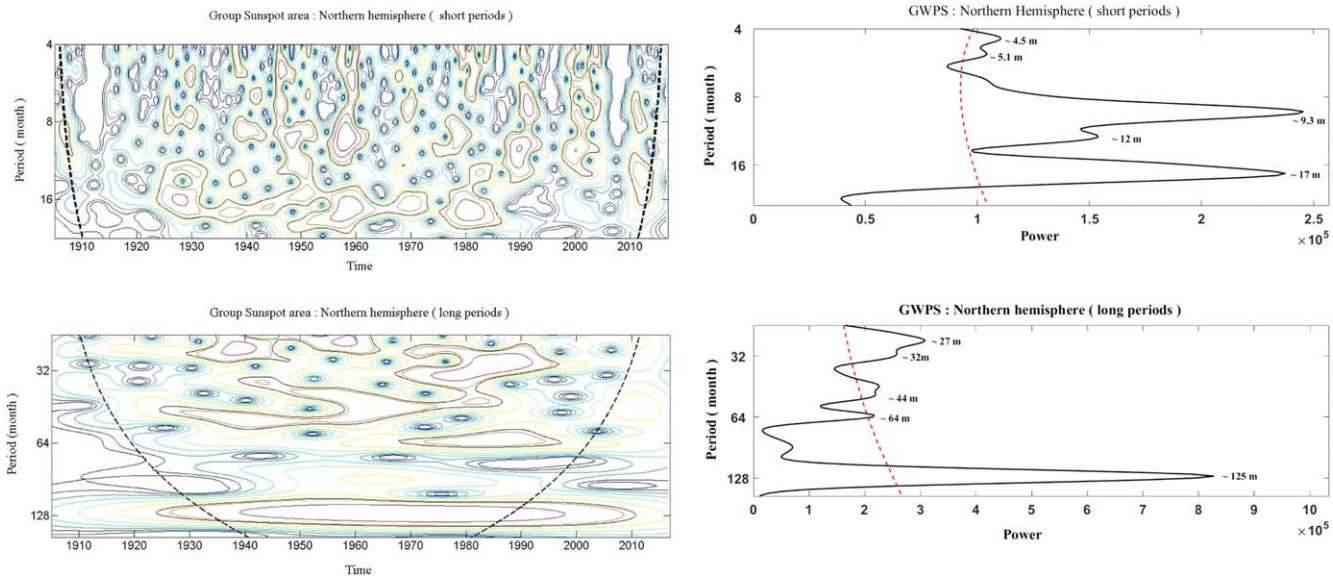

Figure 8. (a) Morlet wavelet spectra of the monthly KO sunspot group area time series in the northern hemisphere. (b) Global power spectra for short-term periods mainly to study the Rieger-group periodicities. (c) Local Morlet wavelet power spectra to investigate the dynamical behaviors of QBOs (1.4 to 4 yr) and other long-term periods including the solar cycle period. (d) Similar to panel (b) for other long-term periods including the Schwabe cycle. The dotted lines in all global wavelet power spectra represent the 95% confidence level.

and 22 in the scattered form (Figure 9, top left). We have detected such types of QBOs in the southern hemisphere in scattered form during 1935–1950, ∼1958–1962, and with varying lengths from ∼1976 to 1990 and from ∼1998 to 2004. Figure 10 (top left and bottom left) represents the local wavelet spectrum of the sunspot group area of the whole solar disk. These plots show Rieger and Rieger-type periods in different parts of cycles 17, 19, 20, 21, 22, and 23. We found that QBOs in the range of 1.2–1.5 yr were significant continuously from cycles 16 to 20, 21, 22, and 23 in this time series.

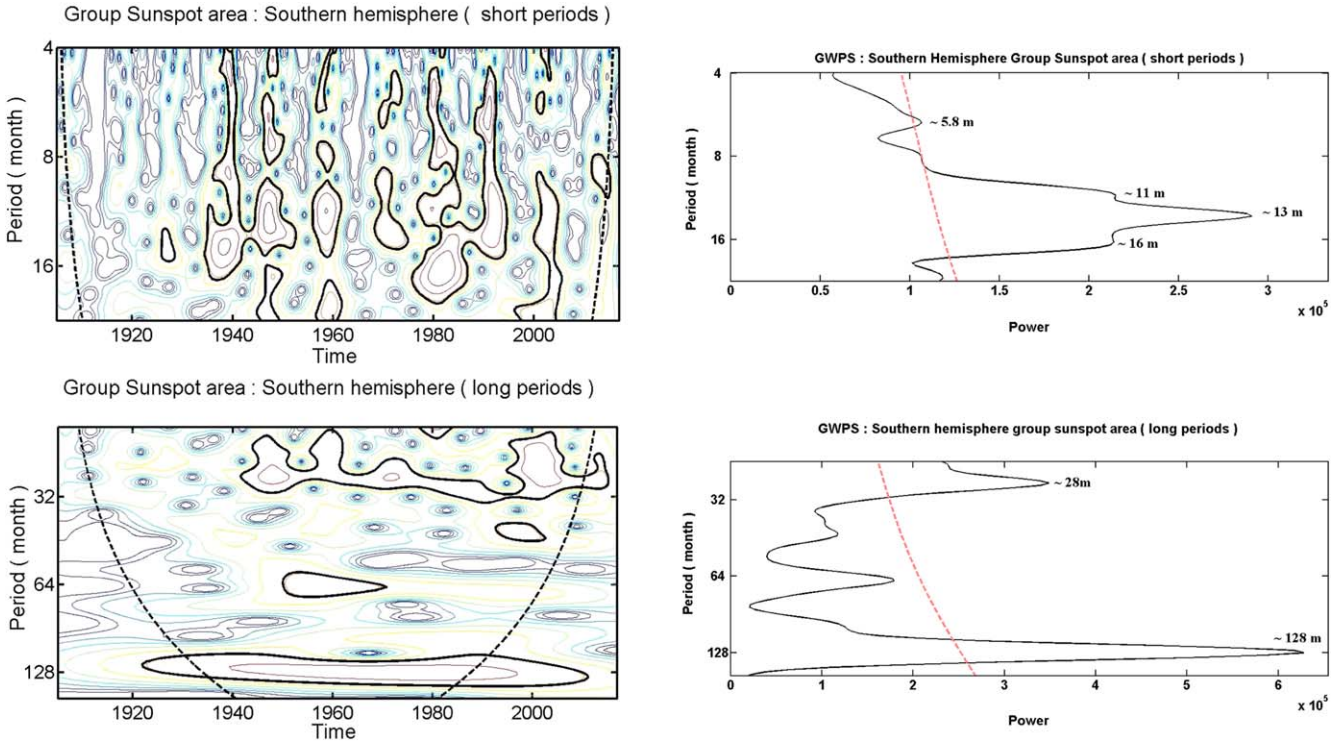

Figure 9. Same as Figure 8, but for the southern hemisphere.

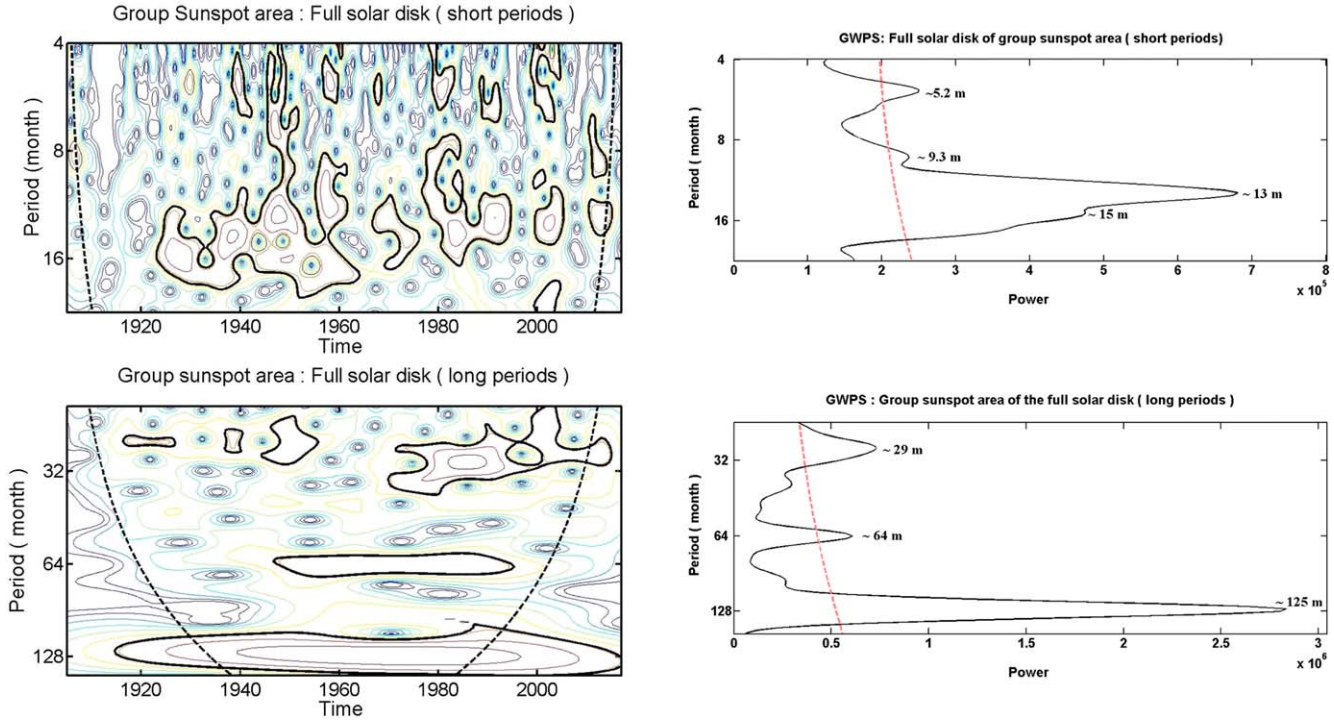

Figure 10. Same as Figure 8, but for the whole hemisphere.

The QBOs in the range of 2–2.5 yr were significant from cycles 16 to 19 and cycles 20 to 22 (Figure 8, bottom left) in the northern hemisphere. This plot indicates the existence of other QBOs (3–4 yr) between cycles 16 and 22. On the other hand, the southern hemisphere shows the presence of only a 2–2.5 yr period from cycles 17 to 24 (Figure 9, bottom left). Solar cycles 16, 18, and 21–24 exhibited the presence of a 2–2.5 yr period for the whole-solar-disk group sunspot area data set (Figure 10, bottom left). A quasi-periodicity of around 5 yr is present in all sunspot group area data sets. The wavelet power spectrum showed the robust existence of solar cycle periodicity in all sunspot area data sets under study.

Figures 8 (top right and bottom right), 9 (top right and bottom right), and 10 (top right and bottom right) represent the

Table 2
Periods Determined Using the GWPS Applied to the KO sunspot Group Area Data for Cycles 14–24

Sunspot Number Data	Major Periods in Months (>95% Confidence Level)
Northern Hemisphere	∼4.5, ∼5, ∼9.3, ∼12, ∼17, ∼27, ∼32, ∼44, ∼64, ∼125
Southern Hemisphere	∼5.8, ∼11, ∼13, ∼16, ∼28, ∼128
Whole Solar Disk	∼5.2, ∼9.3, ∼13, ∼15, ∼29, ∼64, ∼125

GWPS of the corresponding local wavelet plots of the sunspot group area where the peaks of the significant periods are marked. Table 2 shows the results of the GWPS plots.

Table 2 indicates that peaks in the GWPS plots have similarities with the periods of the local wavelet spectra of the sunspot group area time series. Rieger-type periods, QBOs in the range of 1.2–3 yr, the ∼5 yr period, and the Schwabe cycle period (10–11 yr) were prominent in GWPS. To detect the presence and evolution of the ∼22 yr magnetic cycle in the group sunspot area data, we have adopted the same technique as applied in the sunspot number data. Figure 11 displays the wavelet plots, which indicate the presence of the Hale cycle in the hemispheric and full-disk group sunspot area data sets. From the GWPS plots it is clear that the length of this cycle is slightly lower in the southern hemisphere.

3.5. Spatiotemporal Evolution of QBOs (1–2.5 yr)

QBOs in the range of 1.2–2.5 yr are considered as the most prevalent with a quasi-periodicity shorter than the 11 yr sunspot cycle and are related with the double-peak nature of the solar cycle (Hathaway 2015). These groups of periods were detected in different solar and heliospheric activity indices, including helioseismic proxies, asymmetry time series, as well as in the galactic cosmic ray data sets (e.g., Vecchio et al. 2012; Bazilevskaya et al. 2014; Broomhall & Nakariakov 2015; Deng et al. 2019; Ravindra et al. 2021, etc.). It has been reported that QBOs are intermittent in nature without any stable period. The amplitude of the QBOs is modulated in the course of about an 11 yr cycle, being the highest near the maximum solar epoch and becoming weaker during the descending/minimum phase of the solar cycle (Bazilevskaya et al. 2014). Some studies indicated that QBOs during around two years are correlated with the second solar dynamo mechanism (Benevolenskaya 1998; Broomhall et al. 2012; Obridko & Badalyan 2014, etc.).

Here, we have made an effort to study the nature and variations in the QBOs in the range of about two years in terms of both the KO sunspot number and sunspot group area time series. To retrieve the QBOs from all data sets under study, we passed the data through a simple passband filter, which consists of a 10 month and a 30 month smoothing with a consequent subtraction of the latter data from the former one following the recipe of Bazilevskaya et al. (2014). Figure 12 (left and right) shows the evolution/nature of the data sets of the sunspot number and the sunspot group area after using the above-mentioned filters, respectively. Next, we have applied the Morlet wavelet tool on these extracted data sets considering $\omega_0 = 6$ under a "red-noise background" to explore the spatio-temporal evolution of the QBOs (1.2–2.5 yr). In all cases, we have drawn the plots of GWPS considering the "red-noise background."

3.6. QBOs in Sunspot Number

Figure 13 (top left) represents the evolution of QBOs in the sunspot number data in the northern hemisphere. Periods of length from 1.5 to 2 yr were present from ∼1915 to ∼1925. On the other hand, a big contour of varying length between 1.3 and 2.5 yr was prominent from 1935 to 1980 (during cycles 17–21) and around 2010. In the southern hemisphere these periods were significant during 1910–1925, 1945–1950, and 1960–2015 (covering cycles 19–24; Figure 13, middle left). For the sunspot number of the full solar disk, these periods appeared during 1915–1925, 1930-1940, and 1950–1965 and continually from 1970–2010 (during cycle 20–24; Figure 13, bottom left). These results indicate that the temporal evolution of this group of periods was different in opposite hemispheres. Table 3 shows the results of the GWPS plots of the wavelet analysis.

3.7. QBOs in the Sunspot Group Area

Figure 14 (top left) shows the evolution of QBOs in the sunspot group area in the northern hemisphere. The long contours of varying lengths between 1.3–2.2 yr were significant during cycles 16–22 (1930–1990). Another period of length between 2–2.5 yr was present from 1970 to 1995 (cycles 20 to 23). On the other hand, in the case of the southern hemisphere, these groups of periods were prominent from 1940 to 1995 (cycles 17 to 23) as well as 1976–2015 (cycles 21 to 24) in a different form (Figure 14, middle left). When the full solar disk is considered (Figure 14, bottom left), these groups of periods were present from 1910 to 1960 (cycles 14 to 19) with varying lengths from 1.3 to 2 yr. They again appeared from 1975 to 2015 (cycles 21 to 24), and the length changed from 1.4 to 2.5 yr. The outcome of the GWPS analysis is displayed in Table 4.

Gurgenashvili et al. (2016) have shown that a Rieger periodicity appeared in all solar cycles from 14 to 24 in the sunspot data sets and is strongly correlated with the solar cycle strength. These authors indicated the presence of a periodicity from 185 to 195 days during the relatively weak solar cycles 14–15 and 24 and a periodicity in the range of 155–165 days during the stronger solar cycles 16–23 in the daily sunspot area/number time series measured at the Greenwich Royal Observatory and the Royal Observatory of Belgium (ROB). In this article, we have made an attempt to study the correlation between the QBO length and solar cycle strength considering the sunspot number and group sunspot area of the full solar disk measured at KO. Although, the length of QBOs varies from ∼1 yr to ∼4 yr, we have restricted our analysis for those QBOs whose length varies between 1.2 yr and 2.5 yr. To evaluate the length of the QBO periods during each cycle, we utilized again wavelet analysis in every solar cycle separately of both the sunspot number and group sunspot area full-disk data sets. The QBO periods, which resulted from the GWPS covering an interval of 1.2–2.5 yr and above the 95 % confidence level, are shown in Table 5 and displayed in Figure 15.

Table 5 and Figure 15 show that QBO-type periodicities in the range of 1.2–2.5 yr are not directly correlated with the long-term variations in the solar cycle amplitude. However, we have noted that in some cycles both the sunspot number and group sunspot area data display nearly similar QBO-type periods. Cycle 19 had the highest amplitude, and the QBO length is ∼1.4 yr in both data sets. In some relatively strong solar cycles like cycles 18, 21, and 22, the length of the QBOs vary between 2 and 2.5 yr. On the other hand, some weak cycles (15, 23, and 24) also

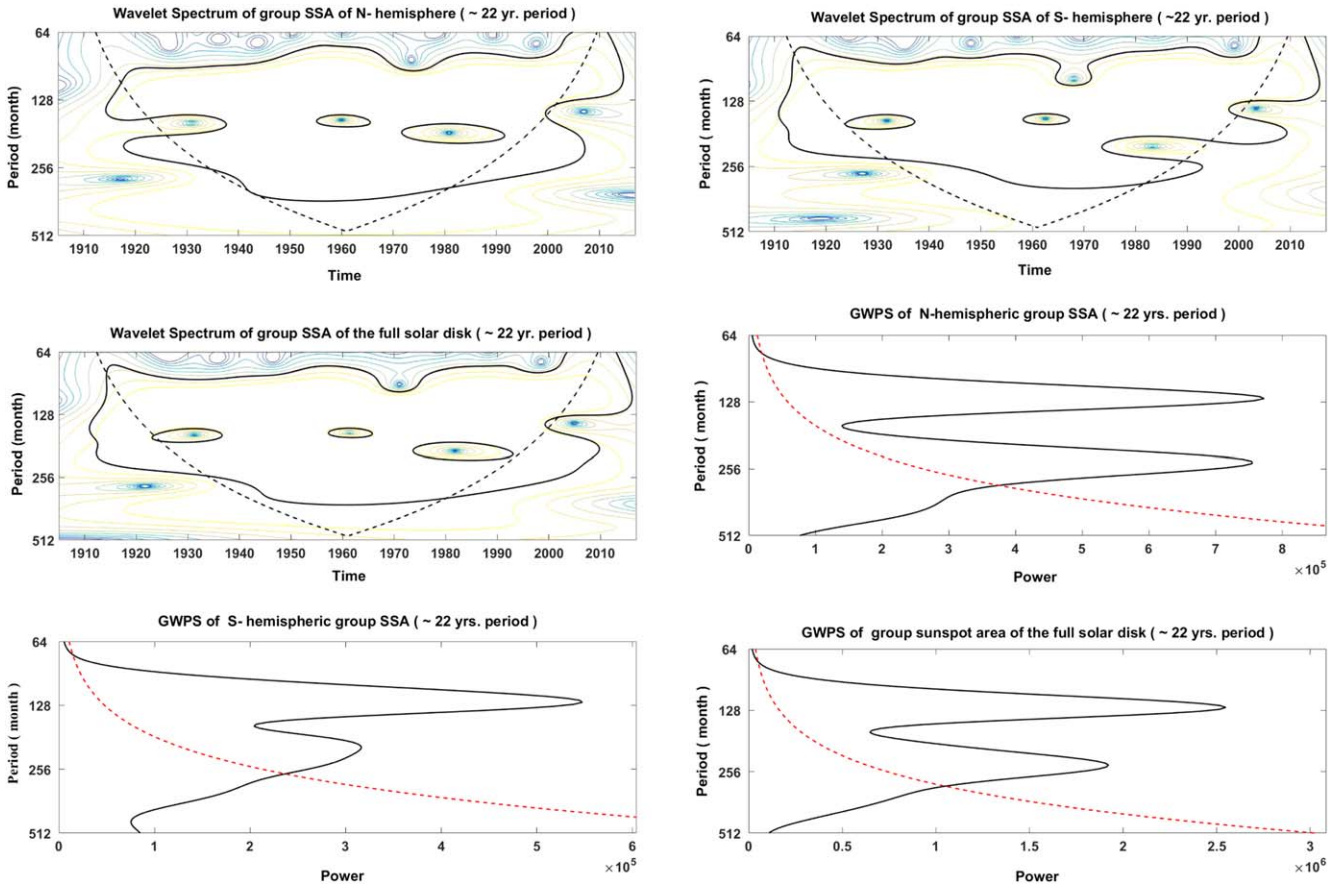

Figure 11. Wavelet plots showing the presence of the ∼22 yr Hale cycle in the hemispheric and full-disk group sunspot area data sets.

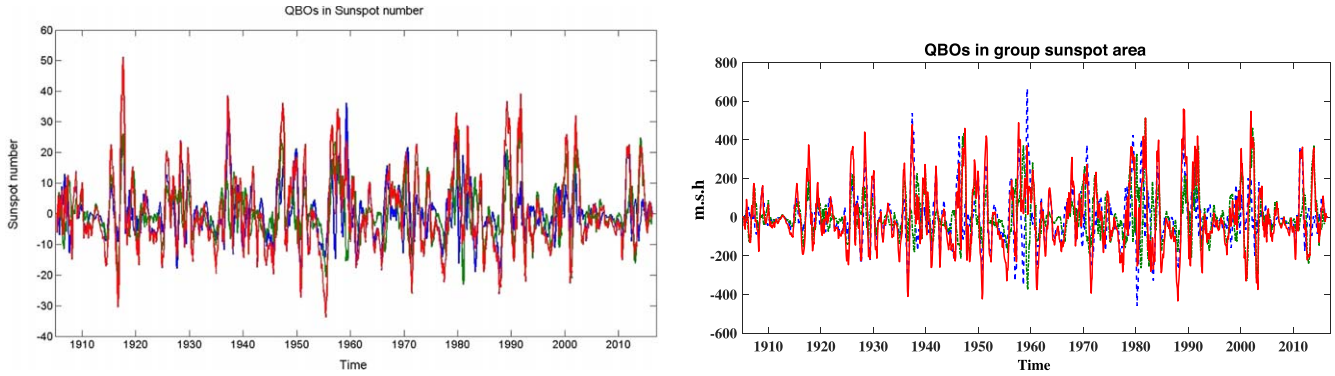

Figure 12. Left: Nature of the QBOs (1.2–2.5 yr), isolated from the KO sunspot number data sets. Right: Same as left-side plot but for the KO sunspot group area time series. In both cases, the "blue" curve is for the northern hemisphere, the "green" curve is for southern hemisphere, and the "red" curve indicates the full solar disk.

possessed similar QBOs (∼ 2–2.5 yr). The most significant QBO for cycle 16 is ∼1.3 yr, and this cycle is a weaker one, which contradicts with the results of the strongest cycle 19. Hence, with the KO sunspot data sets we did not detect any direct correlation between the cycle strength and the QBO length.

4. Model Fitting and Statistical Significance Tests

In the previous sections, we have determined different properties as well as periodic and quasiperiodic variations present in the KO sunspot number/group sunspot area data sets. To find the reliability of the significance levels of these periodicities, we have performed a model fitting the data sets using the autoregressive model (AR model; Box & Jenkins 1970; Chatfield 2001). For this purpose we have applied the ARIMA model (Montgomery et al. 2015), which was previously used to build different models for time-series analysis and cycle-strength forecasting (Abdel-Rahman & Marzouk 2018). The goodness of fit of the model has been checked with the Kolmogorov–Smirnov (K-S) and Anderson–Darling (AD) tests. The AD test (Stephens 1974) is a robust statistical analysis, which is used to test if a sample of data (here the sunspot number and area) occurs from a population following any specific distribution. It is a modified version of the K-S test and provides more weight to the tails of the distribution than the K-S test. We have utilized the generalized ARIMA (p, d, and q) model, which is a mixed integrated model, where p is the number of lag observations in the model (lag order), q indicates the size of the moving average

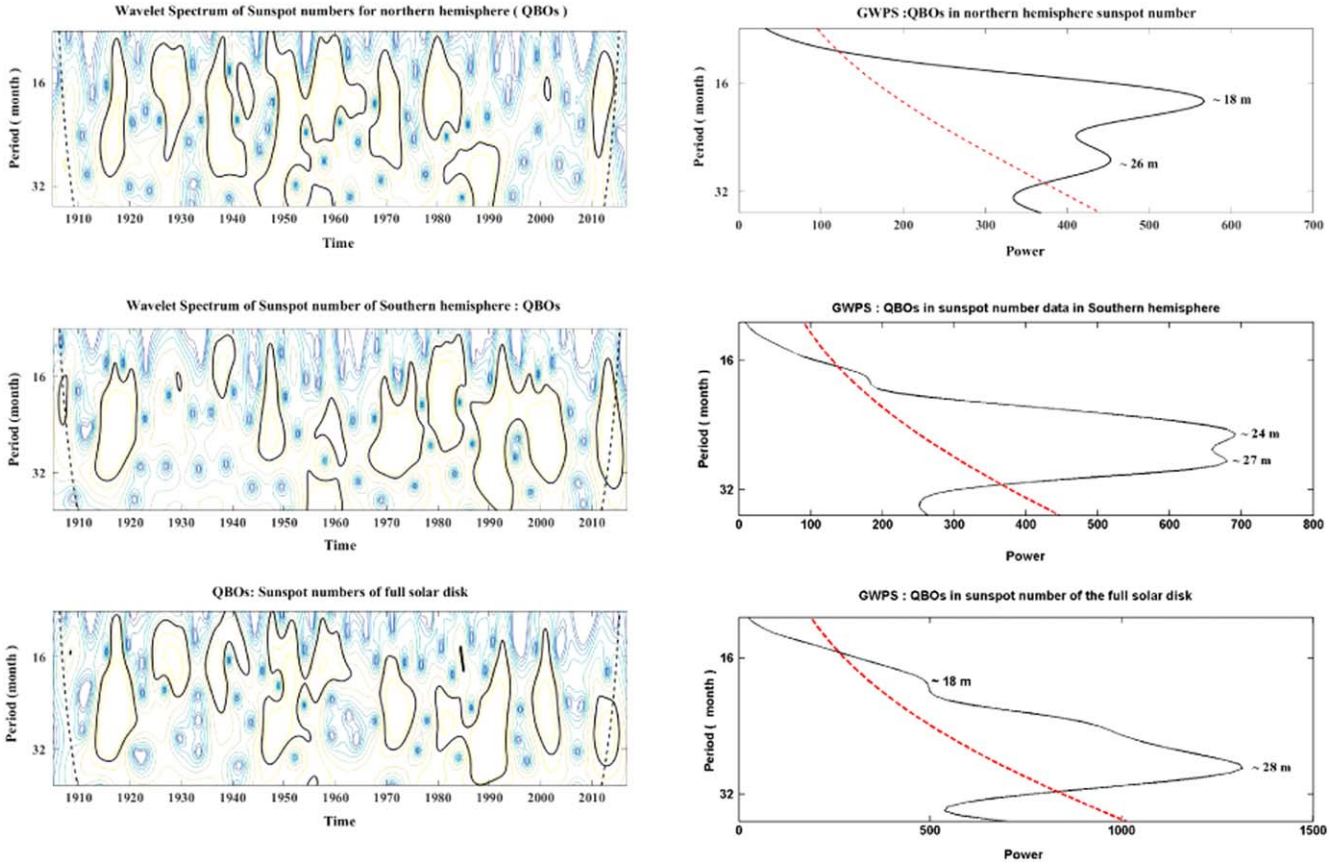

Figure 13. Top left: Morlet wavelet spectra of the northern hemispheric sunspot number data as derived from Figure 12 (top left) to study the nature and evolution of the QBOs (1.2–2.5 yr). Top right: GWPS of the Figure 13 (top left). Middle left: Same as top left, but for the southern hemisphere data. Middle right: GWPS of middle left. Bottom left: Same as top left, but for full-disk data. Bottom right: GWPS of bottom left plot.

window (order of the moving average), and d represents the number of times that the raw observations are differenced to make the time series stationary (degree of differences).

In the ARIMA model, $d = 1$ means taking the differences in the series only once (differences is first order) and the difference continue up to the series stationary, i. e., $d = 1, 2, 3, \ldots$ etc. The main aim of this model is to investigate the past observations of any time series carefully and rigorously to develop an appropriate model that can forecast future values for the series. We have determined the Akaike information criterion (AIC), which is an estimator of the prediction error, the Akaike information corrected criterion (AICc), and the Bayesian information criterion (BIC) for each of the data sets under study. The AIC and the BIC measure the performance of the fitted model, i.e., the goodness of fit and its complexity (Kass & Raftery 1995). A detailed description about the abovementioned statistical tests/models is available in Hyndman & George (2021). Below, we have provided the results of different statistical tests.

Before applying the ARIMA model, we have used BOX-COX transformation of all the data sets (time series) under study and have padded all missing data by one as all data need to be positive.

4.1. ARIMA Model Fitting and Residue Analysis of the Sunspot Number

After performing the BOX-COX transformation (with optimal lambda = 0.384) for the northern and southern hemispheric sunspot number data, we modeled the northern hemisphere using ARIMA(3, 0, 2) and the southern hemisphere using ARIMA (1, 0, 2) and obtained the minimum values of AIC, AICc, and BIC. After this, we performed the AD normality test using the residue of the ARIMA model as the input data and obtained the values of A (test statistic) and p-value. The two-sample K-S test is also performed on the data of the residue of the ARIMA model and the random normal data (two-sample test) and obtained the D values (test statistic) p-values from the test. All these values are listed in Table 6 for the northern and southern hemispheric sunspot number data sets. The obtained values show that the null hypothesis is true, which means that standardized residues may be considered, which is nothing but white noise drawn from $N(0,1)$.

4.2. ARIMA Model Fitting and Residue Analysis of the Group Sunspot Area Data

A similar analysis is done on the sunspot group area data as well. After performing the BOX-COX transformation with optimal $\lambda = 0.210$ ($\lambda = 0.303$) for the northern (southern) sunspot group area, we modeled the northern (southern) hemispheric data using ARIMA(1,1,3) (ARIMA(2,1,2)). The values obtained for this model, the AD test, and the K-S test data are shown in Table 7.

The AD test indicates that the null hypothesis is rejected, which means that the standardized residues cannot be thought as white noise drawn from $N(0,1)$. However, the K-S test states that the null hypothesis may be considered true, and this means

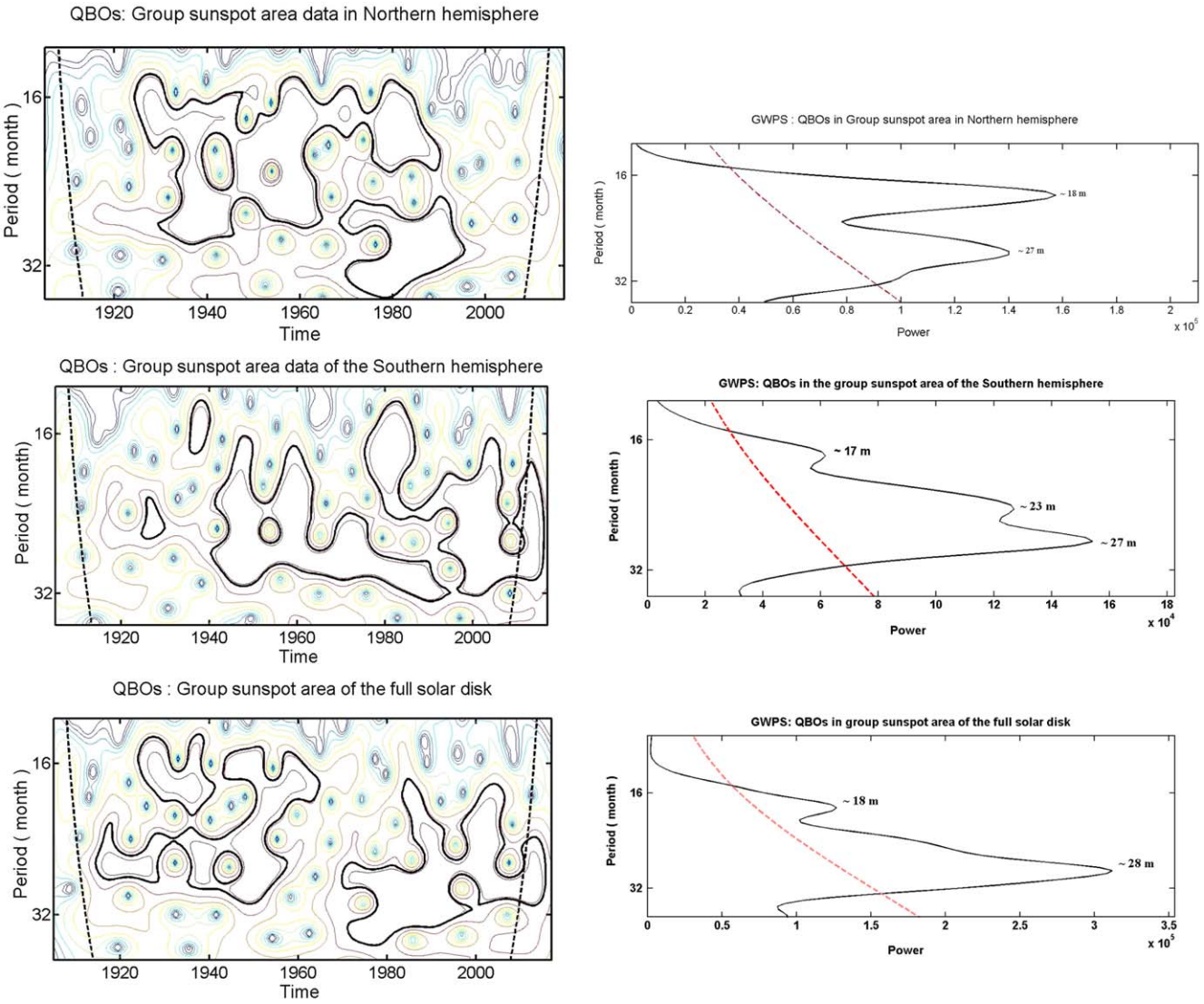

Figure 14. Same as Figure 13, but for the sunspot group area data.

Table 3
QBOs Determined Using the GWPS Applied to the KO sunspot Number Data for Cycles 14–24

Sunspot Number Data	Major Periods in Months (>95% Confidence Level)
Northern Hemisphere	∼18, ∼26
Southern Hemisphere	∼24, ∼27
Whole Solar Disk	∼18, ∼28

Table 4
QBOs Determined Using the GWPS Applied to the KO sunspot Group Area Data for Cycles 14–24

Sunspot Number Data	Major Periods in Months (>95% Confidence Level)
Northern Hemisphere	∼18, ∼27
Southern Hemisphere	∼17, ∼23, ∼27
Whole Solar Disk	∼18, ∼28

that standardized residues may be considered to be nothing but white noise drawn from $N(0,1)$.

5. Wavestrapping Analysis of Sunspot Activity

From Figures 2 and 3, we have found several spatio-temporal properties of the sunspot number and group sunspot area of both hemispheres as well as for the full solar disk. Our wavelet analysis also detected a number of midterm quasi-periods including the well-known ones of ∼11 and ∼22 yr. To assess the significance of the sample cross correlation between two time series, i.e., the northern and southern hemispheric sunspot number/group sunspot area, we have used the wavestrapping method (Percival 2001). Wavestrapping is an important sampling method in the wavelet domain, which joins two major concepts in the statistical signal processing: wavelet analysis and bootstrapping. This statistical tool is mainly appropriate for those time series that exhibit long-term memory properties, i.e., correlation over long periods. The classical Fourier analysis method distinguishes the frequency components of a signal/time series, whereas wavelet analysis considers the signals whose frequency components change over time. Wavelets are basically some "little waves" that are finitely extended, and this technique decomposes a signal/time series in an orthonormal basis of these wavelets (Ogden 1997; Torrence & Compo 1998, etc.). On the other hand,

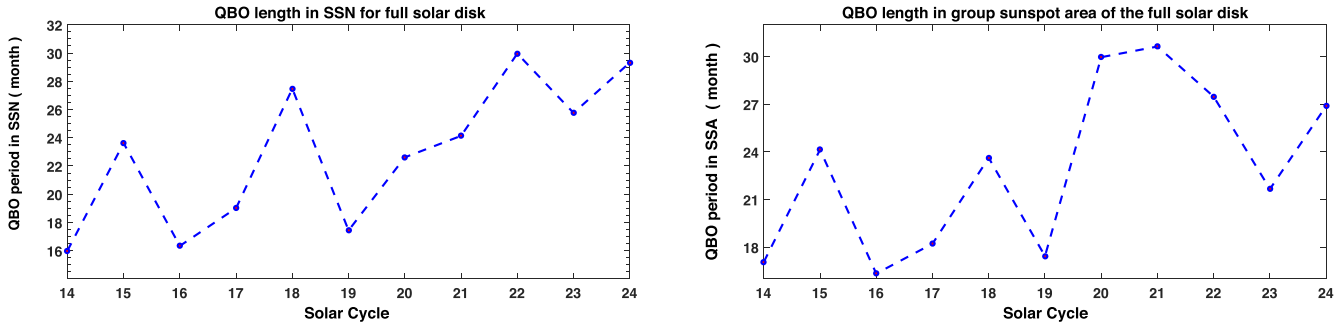

Figure 15. Display of the QBO length and cycle strength.

Table 5
QBOs Seen in the Sunspot Number and Area of Each Cycle

Cycle No.	T-SSN QBO (months)	Average SSN	T-SSA QBO (months)	Average group SSA (m.s.h)
Cycle 14 (decay phase)	15.9	58.9	17.1	435.04
Cycle 15	23.6	73.3	24.13	497.27
Cycle 16	16.7	68.24	16.32	689.10
Cycle 17	19.01	96.07	18.21	880.54
Cycle 18	27.47	108.89	23.62	914.23
Cycle 19	17.43	129.10	17.78	1398.36
Cycle 20	22.61	86.88	29.96	968.30
Cycle 21	24.134	111.40	30.63	1245.77
Cycle 22	29.96	106.73	27.47	1147.8
Cycle 23	25.758	82.23	21.66	955.40
Cycle 24	29.32	64.35	26.89	694.48

bootstrapping is a resampling technique with replacement from the observed data and makes use of the resampled sequences to evaluate the properties of a given estimator through its empirical distribution, without any pre-assumption of any kind of theoretical distribution (e.g., Gaussian/exponential distribution; Robert & Casella 2018). In this technique, the simulation is done by the random selections of the events from the original experimental data set with returning them back to the initial experimental set. Here, the selection of any particular event from the original data set can be done many times or even not for a single time. This method is widely applied for the calculation of the statistical errors of any data set when its direct evaluation is difficult or not realizable at all. The bootstrap methodology provides different types of confidence intervals like normal representation, basic, percentile, BCa (bias-corrected, accelerated). Barbe & Bertail (1995) have provided a detailed description of the bootstrap method. Here, we have applied the bootstrapping method between the north and south hemispheric sunspot number data. The cross correlations between the north and south data have been calculated after taking 10,000 samples generated from the north and south hemispheric sunspot number time series by the bootstrap method. We have made plots of the histogram of the bootstrap-generated sample cross correlation and the Q–Q plot of the generated cross-correlation data (Figure 16).

5.1. Bootstrap Statistics

After taking the 10,000 samples of the sunspot number data generated by the bootstrap method, we have computed the cross-correlation value, and it is found to be 0.72 with a bias of −0.0002 and a standard error of 0.013. This analysis provided the confidence intervals for the normal representation at the 95% level as (0.6949, 0.7477) and (0.6956, 0.7481) in the basic level and in the BCa representation (0.6941, 0.7465) and (0.6937, 0.7462) at the level percentile.

Table 6
Values of AIC, AICc, and BIC Obtained after Using the ARIMA(3, 0, 2)/ARIMA(1, 0, 2) Models, AD Normality Test, and K-S Test for the Northern/Southern Hemispheric Sunspot Number Data

	ARIMA(p, d, q)			AD		K-S	
SSN	AIC	AICc	BIC	A	p	D	p
NH	5333.38	5333.44	5364.59	0.364	0.439	0.018	0.982
SH	5447.83	5447.87	5473.83	0.573	0.136	0.022	0.891

This analysis of the cross correlation of the north and south data sets indicates that these two data sets are dependent to some extent on each other. For this reason some small/midterm periods may appear commonly to both set of data. Wavestrapping is also done by using the bootstrapping method between the north and south hemispheric group sunspot area data. The cross correlations between the north and south group area data have been calculated taking 10,000 samples generated from the north and south area data sets as done previously, and the relevant plots are shown in Figure 17.

We have performed similar statistics on the hemispheric sunspot group area data. The analysis shows that the original cross-correlation value is 0.526 with a bias of 9.181×10^{-5} and standard error of 0.022. The intervals of estimation of the cross-correlation analysis done by different methods gave a value at the 95% confidence level as (0.483, 0.569) and (0.484, 0.571). The BCa level values at the same 95% confidence level are (0.482, 0.568) and (0.481, 0.567). The results of this analysis indicates that the northern and southern sunspot group area data sets are dependent on each other to some extent.

5.2. Dynamic Time Warping Analysis of the Sunspot Activity

Dynamic time warping (DTW) is a powerful statistical method to compare the similarities between two varying time series that have nearly similar patterns but differ in time, i.e., do not synchronize up perfectly (Keogh & Pazzani 2001; Müller 2007; Zhang et al. 2021, etc.). This technique is utilized to determine the optimal matching between two sequences. This algorithm was initially developed for speech-recognition purposes (Myers et al. 1981), but nowadays it is widely used in many other scientific domains like meteorology, data mining, financial markets. The DTW algorithm compares the amplitude

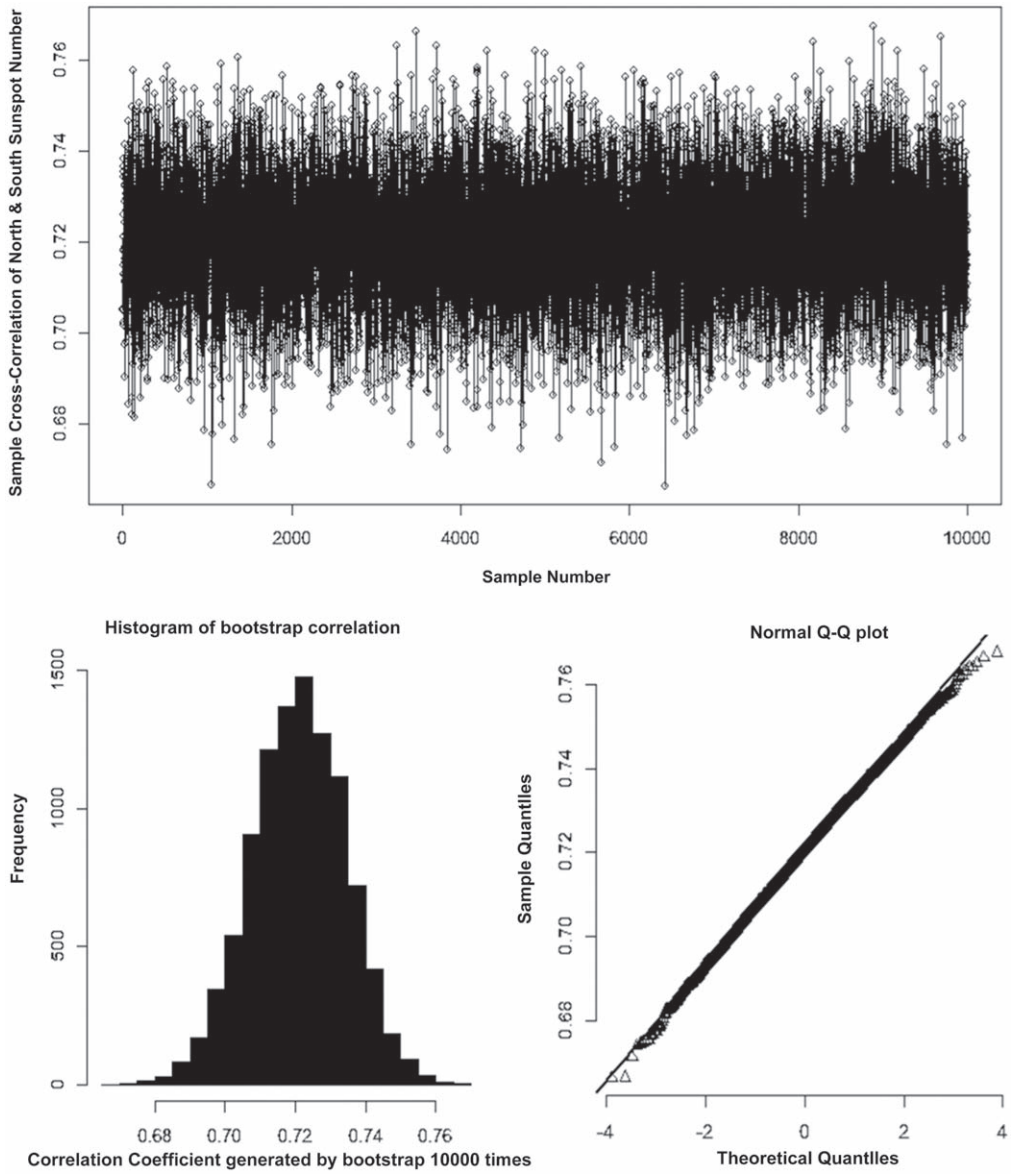

Figure 16. Top: Cross correlation between the sample north and south hemispheric sunspot number time series generated by the bootstrap method. Bootstrap for the sunspot number. Bottom left: Histogram of bootstrap-generated cross correlations. Bottom right: Q–Q plot of the generated cross correlation data.

Table 7
Values of AIC, AICc, and BIC Obtained after Using the ARIMA(1, 1, 3)/ARIMA(2, 1, 2) Models, AD Normality Test, and K-S Test for the Northern/Southern Hemispheric Group Sunspot Area Data

	ARIMA(p, d, q)			AD		K-S	
SSN	AIC	AICc	BIC	A	p	D	p
NH	6407.5	6407.55	6433.51	1.659	0.00029	0.0334	0.442
SH	7715.67	7715.71	7741.68	0.955	0.015	0.0307	0.551

of the first time series at time "t" with the amplitude of the second time series at time $t+1$ and $t-1$ or $t+2$ and $t-2$, which makes sure it does not provide a low similarity score for two time-varying signals of similar shape with different phases (Young-Seon et al. 2011). This technique follows the rule of monotonicity and continuity, with the fact that the first and last points of one signal should be matched with at least the first and last points of the other signal (see Gulzar 2018, for details). It measures a cumulative cost, the DTW score, which exhibits the cost of aligning of two time series in time when their patterns are similar but differ in time (Görecki & Luczak 2013). The DTW technique computes the distance from the matching of similar elements between two time series with the same or different lengths, and this distance is called the "Manhattan distance." The Manhattan distance between two points $x = (x_1, x_2, ..., x_n)$ and $y = (y_1, y_2, ..., y_n)$ in the n-dimensional space is defined as the sum of the distances in each dimension.

$$d(x, y) = \sum_{i=1}^{n} |x_i - y_i|. \quad (4)$$

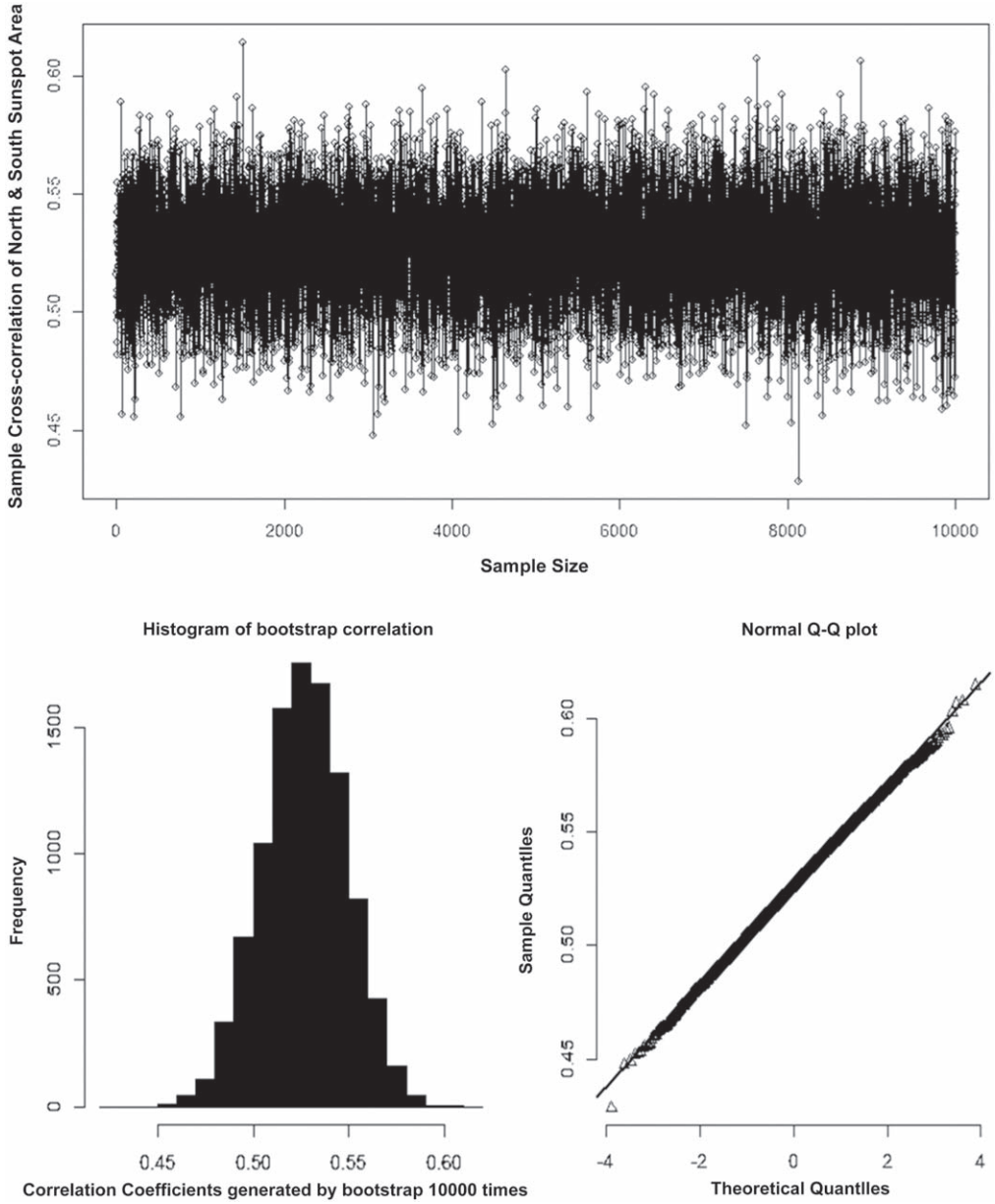

Figure 17. Same as Figure 16, but for the group sunspot area data.

If two sequences of data sets are the same, then the minimum distance between them is zero. However, when the sequences of data are different, then the minimum distance between them is nonzero, and this Manhattan distance increases with the dissimilarity between the data sets (Ratanamahatana & Keogh 2004).

Laperre et al. (2020) used this method to evaluate the geomagnetic storm index Dst forecast with a machine-learning technique. Recently, Samara et al. (2022) have adopted the DTW technique to quantify the similarities and dissimilarities between the observed and modeled solar wind time series forecasting. Here, we are using this technique to determine the Manhattan minimum distance for the two time series of sunspot indices, and Figures 18–19 display the relevant DTW plots.

1. For the north and south sunspot numbers: The Manhattan minimum distance found is 17,029.34, which is quite large and indicates that these two time series are different from one another, though some dependency appears.
2. For the north and south group sunspot areas: The Manhattan minimum distance is 264,008.5, which is also quite large and indicates that these two time series are different from one another, though some dependency is seen in the wavestrapping analysis.

6. Conclusions and Discussions

Sunspots are one of the key components of the solar-surface magnetic field and its variations in the course of time (Norton et al. 2014; Hathaway 2015). This index of spatiotemporal evolution helps us understand the physics behind the solar magnetic field, which is the main driving force of all types of activities inside the Sun. In this work, we have considered the time series of the sunspot numbers and sunspot group area measured from the Sun charts at the Kodaikanal Observatory to investigate the presence and spatiotemporal behavior of the midterm quasi-periodicities as well as the QBOs during solar

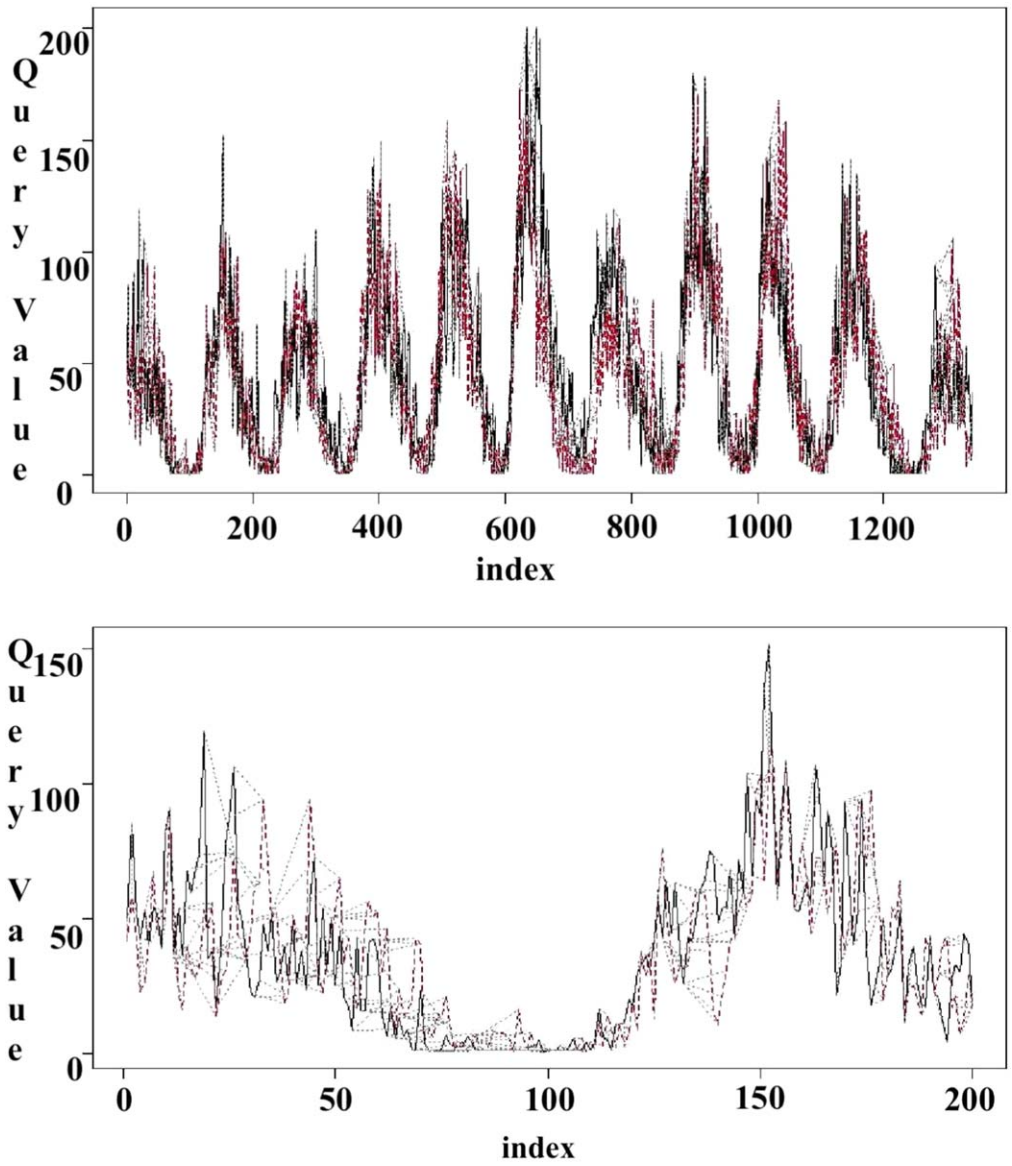

Figure 18. Upper panel: The DTW of the northern hemispheric sunspot number (quarry data, black color) and the southern hemispheric sunspot number (reference data, red color) are mapped to find the minimum distance between these two sets of data sequences. This mapping is shown more clearly for the first 200 sequences of the data (depicted in the lower panel).

cycles 14–24. The search of midterm periods and their time evolution in the Sun and their properties can provide useful information on the global magnetic properties of the Sun (Vecchio & Carbone 2009) like the working behavior of the complex dynamo in different solar cycles. Along with it, the nonconstant periodic lengths less than the Schwabe cycle ($\sim$ 11 yr) could enrich the "solar melody" (Beer et al. 1994) with additional components, affecting the space weather/climate and our human activities (Temmer 2021). This is the first investigation to detect the periodic and quasiperiodic variations present in this handwritten long-term sunspot data set measured at the KO covering about 11 sunspot cycles, cycles 14–24. We have applied the wavestrapping and DTW methods to determine the statistical relationship between the northern and southern hemispheric sunspot activity data sets. We provide a summary of the main findings of our study with discussions:

1. It is revealed that both the amplitude and temporal variation in the KO sunspot number and sunspot group area are not the same in the northern and southern hemispheres. The behavior of the ascendant phase, peak time, and decay rate is also different in both hemispheres in several solar cycles. We observed the maximum amplitude of the sunspot numbers during solar cycle 19 in both hemispheres, and the sunspot number amplitude of the whole solar disk is the minimum during cycle 16 for the northern hemisphere, which is comparable with the strength of cycle 24 in the same hemisphere. However, in the case of the southern hemisphere, cycle 20 is the weakest one. Solar cycle 24 showed the timidest attitude for the whole-solar-disk data. The dynamical behavior of the KO sunspot number has strong similarities with the recently prepared hemispheric sunspot number from different solar proxies (Veronig et al. 2021) and so may be considered as an alternate proxy of the international sunspot number for long-term hemispheric solar cycle studies.

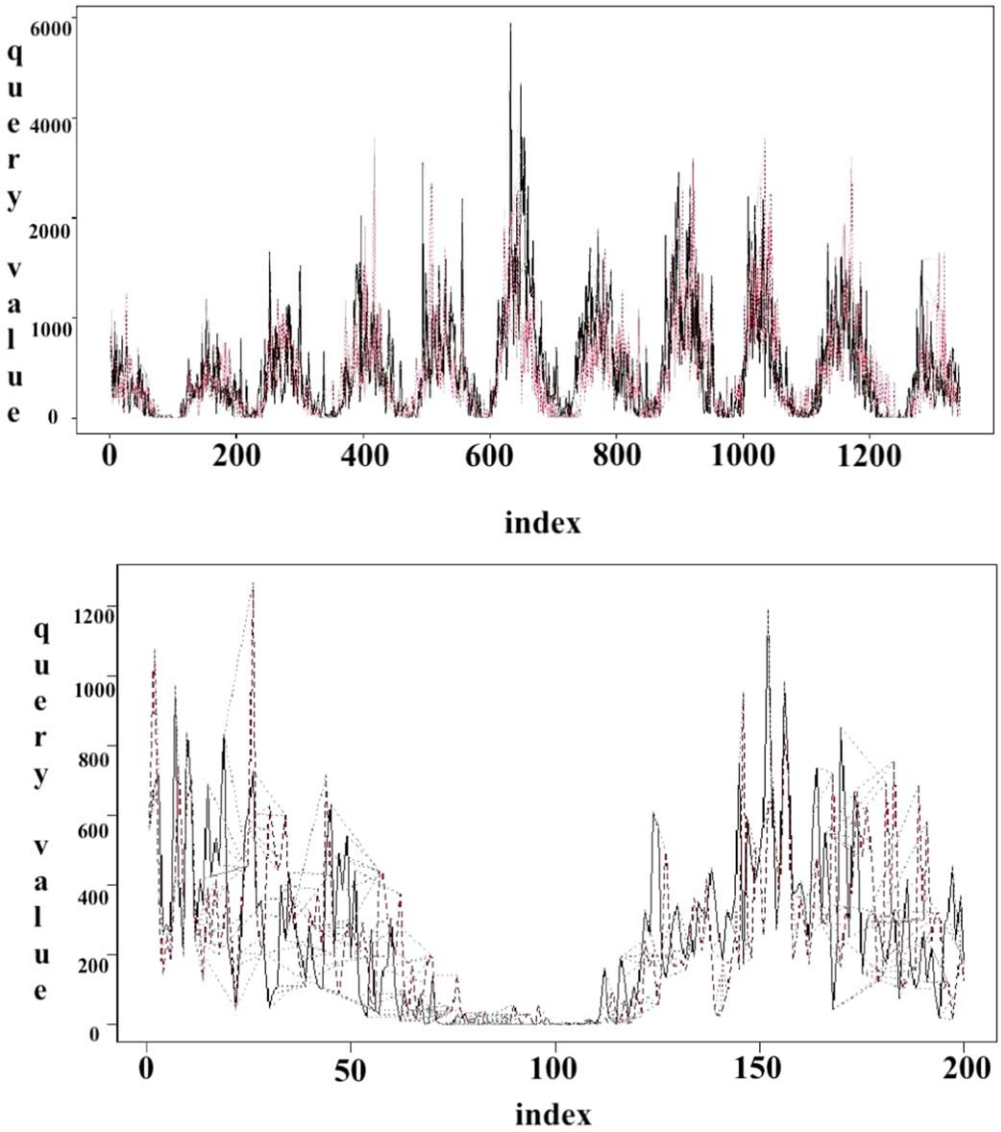

Figure 19. Upper panel: The DTW of the northern hemispheric sunspot area (quarry data, black color) and the southern hemispheric sunspot area (reference data, red color) are mapped to find the minimum distance between these two sets of data sequences. This mapping is shown more clearly for the first 200 sequences of the data (depicted in the lower panel).

2. For the sunspot group area index, both the hemispheric and full-disk data exhibit the maximum amplitude during cycle 19. Cycle 15 showed the weakest amplitude in both hemispheres. For the whole sphere, the amplitude of both cycles 15 and 24 showed a nearly equally weak nature.
3. Double peaks are found around the maximum episode of many solar cycles for both the sunspot number and sunspot group area. However, the nature of the double peak is different in different solar cycles and opposite hemispheres. This nature is consistent with the temporal evolution of the recently digitized sunspot area as well as the Ca–K plage index data set measured at the KO (Ravindra et al. 2021; Chowdhury et al. 2022).
4. Sunspot number data measured at Royal Greenwich Observatory (RGO) as well as in the KO indicate that the amplitudes of cycles 16, 18, and 20 are smaller than that of the immediate odd-numbered cycle and hence follows the odd–even rule (Ravindra et al. 2021; Chowdhury et al. 2022). This rule has been violated for the cycle 22–23 pair. Similar behavior is also found for the sunspot group area time series. The full-disk data set of the sunspot number and area indices exhibits a weakening nature from solar cycle 21 to 24.
5. The Morlet wavelet analysis method detected several intermediate-term periodicities, including the well-known Rieger and Rieger-group periodicities and the QBOs, separately in the northern and southern hemispheres and full disk for both the sunspot number and group sunspot area data sets. However, we noticed that the temporal evolution and amplitude of these periods are different in opposite hemispheres in both data sets. We have made a detailed investigation about the spatiotemporal evolution of QBOs in the range of 1.2–2.5 yr and observed that these groups of QBOs have some north–south asymmetry in existence in both sunspot numbers and sunspot group area time series. Distinctive peaks around 1.5 yr and around 2.2 yr were found in all data sets under study. Thus, QBOs ∼2 yr were significant in both the sunspot indices measured at KO. However, we have seen that the modulation and appearance of these periods are different

in opposite hemispheres. We have detected the signature of about a 5 yr quasi-periodicity, which was much prominent in the sunspot number data of the southern hemisphere and the full solar disk. This period is prominent and persisted for a long time only in the full-solar-disk sunspot group area data. We found that all these data sets under investigation have prominent 10–11 yr cyclic variations. Along with it, we have also detected the presence of a ∼22 yr period in both data sets, which reflects the inversion of the polar magnetic field. However, we did not find any direct connection between the length of the QBOs in the vicinity of ∼2 yr and the solar cycle strength for the full-solar-disk data sets.

6. We have applied the nonstationary ARIMA model to fit the sunspot number and group sunspot area time series and checked the goodness of fit. We have found that the data sets are fitted in the ARIMA model, and the K-S test states that the null hypothesis may be considered true, and the standardized residues of the data sets may be considered as white noise.
7. In this investigation, we have utilized two alternative ways of assessing the performance of hemispheric sunspot activities, the so-called wavestrapping/bootstrapping and DTW techniques. The wavestrapping methodology indicates that the northern and southern hemispheric sunspot data sets are dependent to some extent on each other. The DTW technique indicates that, although the Manhattan minimum distance between opposite hemispheres is quite large, these two time series are different from one another, though some dependency was observed.

In the present work, we have used a complex Morlet wavelet analysis tool to detect the intermediate-term periodicities (>3 months to ⩽11 yr) in the sunspot number and sunspot group area data sets measured at KO (Hathaway 2015). A periodicity of about 11 yr normally dominates the sunspot cycles. Along with other periods, the most significant and persistent periods, which several researchers reported, are 130–190 days (Rieger-group/type periods) and 1.3–2.5 yr (Krivova & Solanki 2002; Bai 2003; Knaack et al. 2005, etc.). Rieger-group periods were detected in different solar and interplanetary parameters like the sunspot number/area (Lean 1990; Carbonell & Ballester 1992; Chowdhury et al. 2009, 2019; Kilcik et al. 2014); photospheric magnetic flux (Ballester et al. 2002; Knaack et al. 2005); solar flares and coronal mass ejections (Lou et al. 2003; Choudhary et al. 2014; Kilcik et al. 2020); solar energetic particle events (Richardson & Cane 2005; Chowdhury & Ray 2006; Laurenza et al. 2009; Richardson et al. 2016); north–south asymmetry of sunspot activities (Chowdhury et al. 2013; Ravindra et al. 2021, etc.). These studies indicated that Rieger-type periodicities are not recognized as typical of every sunspot cycle but seem to appear only in different phases of some cycles. These Rieger-group periods were detected in our sunspot activity data sets with intermittent nature, as discussed in Sections 3.3 and 3.4.

QBOs in the range of 1.2–4 yr, although weaker than the main cycle (∼11 yr period), are very robust as they have been noted in many solar activity indicators for the last two decades (e.g., see Table 1 in Bazilevskaya et al. 2014). QBOs in the range of 1.3–2 yr were also detected in high-latitude (⩾60°) polar faculae (Deng et al. 2020) as well as in the frequency shifts of the helioseismic data (Komm et al. 2000; Simoniello et al. 2013; Broomhall & Nakariakov 2015). The temporal variations in the helioseismic proxies are also associated with the changes in the solar internal magnetic fields. Recently, Inceoglu et al. (2021) reported the presence of QBO-like signals of ∼2 yr in different latitudinal bands in the rotation rate residuals at different depths of the deep solar interior. Our wavelet analysis has shown the prominent presence of QBOs in both hemispheres and in the whole-solar-disk data of the sunspot number and sunspot group area time series with some intermittency. The QBOs exhibit length variation and appear in the opposite hemispheric data sets at different times. These findings indicate that the QBOs is one of the most prevalent quasi-periodicities among sunspot activity indices.

The turbulent α-dynamos are assumed to be the mechanism responsible for the generation of the QBOs in the range of 1.3–2.5 yr (Inceoglu et al. 2019). We have detected the quasi-periodicity of about 5 yr, which was previously detected in the century-long digitized Ca–K plage index (Chowdhury et al. 2016, 2022) and sunspot area time series (Ravindra et al. 2021) measured at KO. This period, which is a harmonic of the 11 yr sunspot cycle, is probably closely related to the double-peak behavior of the solar cycles (Georgieva 2011; Hathaway 2015). The 11 yr periodicity is the strongest period determined in all of the sunspot activity data sets under investigation and is probably connected with the global dynamo mechanism (Charbonneau 2020). The detection of the ∼22 yr period in both the sunspot indices provides a strong evidence for the existence of a relic magnetic field in the Sun. Further, we have made an effort to determine any correlation between the length of QBOs (1.2–2.5 yr span) and the strength of the solar cycle considering both the sunspot number and the group sunspot area data sets in each solar cycle under study, but failed to find any such direct connection. In the near future, we aim to study this phenomenon more rigorously considering the long-term data sets of the hemispheric sunspot number and sunspot area obtained from other observatories including KO.

There is no physical model that can explain the different aspects of the origin and intermittent behavior of the different types of intermediate-term periods found in the solar indices. Bai & Sturrock (1993) and Bai (2003) studied the longitude distribution of major flares for cycles 19–22 and proposed an obliquely rotating structure of wave patterns rotating with a period of 25.5 days about an axis tilted by 40° to the solar rotation axis responsible for Rieger-type periods. However, there exists no observational evidence of such a clock-type rotating structure inside the Sun. On the other hand, Ballester et al. (2002) linked different midterm quasi-periods, especially Rieger ones, with the periodic emergence of magnetic flux from the deep solar interior to the complex active regions in the solar surface.

After investigating the dynamics near the solar tachocline region, Zaqarashvili et al. (2010a) proposed that Rieger-type periods are favored when the magnetic field strength is $\leqslant 10^4$ G in the upper overshoot layer of the tachocline. A magnetic field with strength $\leqslant 10^5$ G near the lower layers of the tachocline leads to oscillations with a period of ∼2 yr (Zaqarashvili et al. 2010b). Some researchers argued that the behaviors of different quasi-periodicities are governed by the dynamics of Rossby-type waves in the solar atmosphere (Lou 2000; Ulrich 2001; Gurgenashvili et al. 2016; Dikpati et al. 2018a; Dikpati & McIntosh 2020). Theoretical studies indicate the possibility of generating Rossby-type waves of various scales in the solar

convection zone, which splits into low-order Rossby waves to fast and slow magnetic Rossby waves under the influence of the magnetic field (Zaqarashvili et al. 2007; Raphaldini et al. 2019). Helioseismological studies show that global-scale equatorial Rossby-type waves may be considered as an essential component of internal solar dynamics (Löptien et al. 2018; Liang et al. 2019). These types of waves are also observed in bright coronal points (McIntosh et al. 2017). It is assumed that Rossby waves in the Sun can partly influence some phenomena in the Earth's atmosphere with periods close to a Rieger-type periodicity (Silva & Lopes 2017).

Zaqarashvili (2018) studied the instability of the magnetic field inside the convection zone and indicated that, under the condition of reduced gravity, global equatorial fast magneto-Rossby waves match well the ∼11 yr solar cycle period. On the other hand, Sokoloff et al. (2020) argued that periods in the range of 5–6 yr might be related to the nonlinearities in the solar dynamo operation as well as the nonharmonic/asymmetric shape of the sunspot cycles. Some studies have shown that different solar intermediate-term periodicities (including Rieger-type and QBOs) could be explained by considering suitable spherical harmonics of magneto-Rossby waves (Knaack et al. 2005; Dimitropoulou et al. 2008; Chowdhury et al. 2013, 2019; Sturrock et al. 2013; Gachechiladze et al. 2019; Bilenko 2020; Dikpati & McIntosh 2020, etc.). Zaqarashvili et al. (2021) made detailed investigations about the dynamical behavior of different kinds of magnetic Rossby waves and their relationship with different solar periodicities.

We have found double peaks in different solar cycles around the maximum phase, and the gap between these two peaks is called the Gnevyshev gap (GG; Gnevyshev 1977). However, this double-peaked nature is not prominent in cycle 19, which exhibited the maximum amplitude. On the other hand, both the sunspot number and group sunspot area data sets for recent cycles 23 and 24 showed prominent double-peaked nature. Both these data sets exhibits step-like decay during cycle 20. Such nature is also prominent during cycle 18 of the sunspot group area time series. A similar type of complex patterns are also observed during cycle 20 in the low-latitude Ca–K plage data sets measured at KO (Chowdhury et al. 2022). This type of dynamical behavior is also detected in the recently constructed long-term hemispheric/full-disk sunspot number by Veronig et al. (2021).

We have noted that the sunspot activities during different cycles are not symmetric in both the hemispheres, and this type of hemispheric imbalance is called "north–south asymmetry" (Temmer et al. 2006; Badalyan & Obridko 2017; Ravindra et al. 2021). The reason for this hemispheric imbalance is under debate, and several mechanisms have been proposed in the literature (Norton et al. 2014; Passos et al. 2014). In addition to that, we also observe that the double peaks, step-like decay, and multiple peaks during the rising/descending phase for a given cycle may occur for a particular hemisphere without having any counterpart of the same in the other hemisphere. The reasons behind the complex nature of some cycles are still under investigation. However, Dikpati et al. (2018b) argued that energy exchange among magnetic fields could generate nonlinear quasi-periodicities, which in turn are related to these spikes and multiple peaks during the descending phase in sunspot indices. In this article we have for the first time adapted and applied the wavestrapping and DTW algorithms for the purpose of evaluating the performance of sunspot time series. Both of these two statistical tools indicate that the sunspot data of the opposite hemispheres are dependent on one another, which might be the reason behind the appearance of a number of common midterm periods in the wavelet analysis.

For time series, the parametric modeling with any type of mathematical formalism is very useful if the irregular nature of the data can be enclosed by the selected mathematical/statistical model. Here, we have applied the ARIMA model to fit our data sets and noted that both sunspot data sets can be modeled by higher-order ARIMA models. Our statistical significance tests like the K-S test and the AD normality test with the residue of the ARIMA model and random normal data indicate that both data sets follow the null hypothesis to some extent and the standardized residues may be considered as white noise. Recently Abdel-Rahman & Marzouk (2018) have investigated some properties of the sunspot number time series observed by the National Oceanic and Atmospheric Administration (NOAA) during the period 1991–2017 and showed that this data set may be fitted with the ARIMA (1, 0, 0) model. However, these authors did not study the goodness of fit of their model. Our results will be helpful for understanding the statistical properties of different kinds of solar data and for forecasting the strength of sunspot cycle.

The long-term evolution of the sunspots on the photosphere reflects the process of the magnetic dynamo from the interior part of the Sun. The spatiotemporal evolution, numerical model fitting, statistical properties, and quasiperiodic variations determined from the century-long sunspot number and sunspot group area data sets measured at the KO provide the information to understand different dynamical properties of the soar magnetic field during the past sunspot cycles when satellite-borne data were absent. These long-term data sets may be utilized to reconstruct the solar irradiance in past solar cycles as well (Dasi-Espuig et al. 2016). A search of all these periodicities, statistical modeling, and an asymmetry study are expected to provide useful information about the evolution of the solar global magnetic field and its reflections on the surface layers. It is assumed that the solar magnetic field is produced by a complex dynamo mechanism that is situated near the base of the solar convection zone. Kinematic dynamo models have shown some success in explaining different complex characteristic properties of the solar cycles (e.g., Cameron et al. 2017; Charbonneau 2020; Hazra et al. 2020). More investigations of the formation of the solar magnetic flux, the behavior of the dynamo in the opposite hemispheres, and the operating mode of Rossby-type waves and their variations are required to understand the intrinsic mechanism responsible for these quasi-periodicities.

We thank the referees for going through the manuscript and providing insightful comments. We thank all of the observers at the Kodaikanal Solar Observatory who have been observing continuously for over a century. We also thank the people who have initiated the digitization program at the Kodaikanal Observatory. We thank Mrs. Arockia Mary Anita for helping with the data extraction and tabulation. We thank Javaraiah J. for valuable comments on the manuscript. P.C. would like to thank Dr. F. Clette and Dr. D.H. Hathaway for valuable discussions during his visits to the USA.

ORCID iDs

Belur Ravindra https://orcid.org/0000-0003-2165-3388
Partha Chowdhury https://orcid.org/0000-0003-3253-9054
Pratap Chandra Ray https://orcid.org/0000-0003-2997-846X

References

Abdel-Rahman, H. I., & Marzouk, B. A. 2018, JAsGe, 7, 175
Babcock, H. D. 1959, ApJ, 130, 364
Badalyan, O. G., & Obridko, V. N. 2017, A&A, 603, A109
Bai, T. 2003, ApJ, 591, 406
Bai, T., & Sturrock, P. A. 1993, ApJ, 409, 476
Ballester, J. L., Oliver, R., & Carbonell, M. 2002, ApJ, 566, 505
Barbe, P., & Bertail, P. 1995, The Weighted Bootstrap (New York: Springer), doi:10.1007/978-1-4612-2532-4
Bazilevskaya, G., Broomhall, A. M., Elsworth, Y., & Nakariakov, V. M. 2014, SSRv, 186, 359
Beer, J., Joos, F., Lukasczyk, C., et al. 1994, in The Solar Engine and its Influence on Terrestrial Atmosphere and Climate, ed. E. Nesme-Ribes (Berlin: Springer), 221
Benevolenskaya, E. E. 1998, ApJL, 509, L49
Bilenko, I. A. 2020, ApJL, 897, L24
Box, G., & Jenkins, G. 1970, Time Series Analysis: Forecasting and Control (San Francisco, CA: Holden-Day)
Broomhall, A. M., Chaplin, W. J., Elsworth, Y., & Simoniello, R. 2012, MNRAS, 420, 1405
Broomhall, A. M., & Nakariakov, V. M. 2015, SoPh, 290, 3095
Cameron, R. H., Dikpati, M., & Brandenburg, A. 2017, SSRv, 210, 367
Carbonell, M., & Ballester, J. L. 1990, A&A, 238, 377
Carbonell, M., & Ballester, J. L. 1992, A&A, 255, 350
Charbonneau, P. 2020, LRSP, 17, 4
Chatfield, C. 2001, Time-Series Forecasting (New York: Chapman Hall/CRC), doi:10.1201/9781420036206
Choudhary, D. P., Lawrence, J. K., Norris, M., & Cadavid, A. C. 2014, SoPh, 289, 649
Chowdhury, P., Belur, R., Bertello, L., & Pevtsov, A. A. 2022, ApJ, 925, 81
Chowdhury, P., Choudhary, D. P., & Gosain, S. 2013, ApJ, 768, 188
Chowdhury, P., Gokhale, M. H., Singh, J., & Moon, Y. J. 2016, Ap&SS, 361, 54
Chowdhury, P., Khan, M., & Ray, P. C. 2009, MNRAS, 392, 1159
Chowdhury, P., Kilcik, A., Yurchyshyn, V., Obridko, V. N., & Rozelot, J. P. 2019, SoPh, 294, 142
Chowdhury, P., & Ray, P. C. 2006, MNRAS, 373, 1577
Dasi-Espuig, M., Jiang, J., Krivova, N. A., et al. 2016, A&A, 590, A63
Deng, L. H., Fei, Y., Deng, H., Mei, Y., & Wang, F. 2020, MNRAS, 494, 4930
Deng, L. H., Zhang, X. J., Li, G. Y., Deng, H., & Wang, F. 2019, MNRAS, 488, 111
Dikpati, M., Belucz, B., Gilman, P. A., & McIntosh, S. W. 2018a, ApJ, 862, 159
Dikpati, M., & McIntosh, S. W. 2020, SpWea, 18, e02109
Dikpati, M., McIntosh, S. W., Bothun, G., et al. 2018b, ApJ, 853, 144
Dimitropoulou, M., Moussas, X., & Strintzi, D. 2008, MNRAS, 386, 2278
Gachechiladze, T., Zaqarashvili, T. V., Gurgenashvili, E., et al. 2019, ApJ, 874, 162
Georgieva, K. 2011, ISRAA, 2011, 437838
Gleissberg, W. 1939, Obs, 62, 158
Gleissberg, W. 1940, Obs, 63, 215
Gleissberg, W. 1943, Obs, 65, 24
Gleissberg, W. 1944, ApJ, 100, 219
Gnevyshev, M. N. 1977, SoPh, 51, 175
Gnevyshev, M. N., & Ohl, A. I. 1948, AZh, 25, 18
Görecki, T., & Luczak, M. 2013, Data Mining and Knowledge Discovery, 26, 310
Grinsted, A., Moore, J. C., & Jevrejeva, S. 2004, NPGeo, 11, 561
Gulzar, M. H. 2018, Comprehensive Guide to Dynamic Time Warping in Python (Chisinau: Lambert Academic Publishing)
Gurgenashvili, E., Zaqarashvili, T. V., Kukhianidze, V., et al. 2016, ApJ, 826, 55
Hathaway, D. H. 2015, LRSP, 12, 4
Hazra, S., Brun, A. S., & Nandy, D. 2020, A&A, 642, A51
Hazra, S., & Nandy, D. 2019, MNRAS, 489, 4329
Hoyt, D. V., Eddy, J. A., & Hudson, H. S. 1983, ApJ, 275, 878
Hyndman, R. J., & George, A. 2021, Forecasting: Principles and Practice (3rd ed.; Melbourne: OTexts), https://otexts.com/fpp3/
Inceoglu, F., Howe, R., & Loto'aniu, P. T. M. 2021, ApJ, 920, 49
Inceoglu, F., Simoniello, R., Arlt, R., & Rempel, M. 2019, A&A, 625, A117
Javaraiah, J. 2012, SoPh, 281, 827
Kass, R. E., & Raftery, A. E. 1995, JASA, 90, 773
Keogh, E. J., & Pazzani, M. J. 2001, in Proc. 2001 SIAM Int. Conf. on Data Mining (SDM), Derivative Dynamic Time Warping (Department of Information and Computer Science University of California) (Philadelphia: SIAM), 1
Kilcik, A., Chowdhury, P., Sarp, V., et al. 2020, SoPh, 295, 159
Kilcik, A., Ozguc, A., Yurchyshyn, V., & Rozelot, J. P. 2014, SoPh, 289, 4365
Knaack, R., Stenflo, J. O., & Berdyugina, S. V. 2005, A&A, 438, 1067
Komm, R. W., Howe, R., & Hill, F. 2000, ApJ, 531, 1094
Krivova, N. A., & Solanki, S. K. 2002, A&A, 394, 701
Kudela, K., Mavromichalaki, H., Papaioannou, A., & Gerontidou, M. 2010, SoPh, 266, 173
Laperre, B., Amaya, J., & Lapenta, G. 2020, FrASS, 7, 1
Laurenza, M., Cliver, E. W., Hewitt, J., et al. 2009, SpWea, 7, S04008
Lean, J. 1990, ApJ, 363, 718
Lean, J. L., & Brueckner, G. E. 1989, ApJ, 337, 568
Liang, Z.-C., Gizon, L., Birch, A. C., & Duvall, T. L. 2019, A&A, 626, A3
Löptien, B., Gizon, L., Birch, A. C., et al. 2018, NatAs, 2, 568
Lou, Y.-Q. 2000, ApJ, 540, 1102
Lou, Y.-Q., Wang, Y.-M., Fan, Z., Wang, S., & Wang, J. X. 2003, MNRAS, 345, 809
Mandal, S., Hegde, M., Samanta, T., et al. 2017, A&A, 601, A106
McIntosh, S. W., Cramer, W. J., Pichardo Marcano, M., & Leamon, R. J. 2017, NatAs, 1, 0086
Montgomery, D. C., Jennings, C. L., & Kulahci, M. 2015, Introduction to Time Series Analysis and Forecasting (2nd ed.; New York: Wiley & Sons)
Morlet, J., Arens, G., Forgeau, I., & Giard, D. 1982, Geop, 47, 203
Müller, M. 2007, Dynamic Time Warping (Berlin: Springer), 69
Mursula, K., Usoskin, I. G., & Kovaltsov, G. A. 2002, AdSpR, 29, 1979
Myers, C. S., Rabiner, L. R., & Rosenberg, A. E. 1981, BSTJ, 60, 303
Norton, A. A., Charbonneau, P., & Passos, D. 2014, SSRv, 186, 251
Obridko, V. N., & Badalyan, O. G. 2014, ARep, 58, 936
Ogden, R. W. 1997, Non-linear Elastic Deformations (Mineola, NY: Dover Publications)
Passos, D., Nandy, D., Hazra, S., & Lopes, I. 2014, A&A, 563, A18
Percival, D. B. 2001, Wavelet Methods for Time Series Analysis (Cambridge: Cambridge Univ. Press), doi:10.1017/CBO9780511841040
Qu, W., Zhao, J., Huang, F., & Deng, S. 2012, AJ, 144, 6
Raphaldini, B., Seiji Teruya, A., Raupp, C. F. M., & Bustamante, M. D. 2019, ApJ, 887, 1
Ratanamahatana, C., & Keogh, E. J. 2004, Third Workshop on Mining Temporal and Sequential Data, 32 (Citeseer)
Ravindra, B., Chowdhury, P., & Javaraiah, J. 2021, SoPh, 296, 2
Ravindra, B., Pichamani, K., Selvendran, R., et al. 2020, Ap&SS, 365, 14
Ravindra, B., Priya, T. G., Amareswari, K., et al. 2013, A&A, 550, A19
Richardson, I. G., & Cane, H. V. 2005, GeoRL, 32, L02104
Richardson, I. G., von Rosenvinge, T. T., & Cane, H. V. 2016, SoPh, 291, 2117
Rieger, E., Share, G. H., Forrest, D. J., et al. 1984, Natur, 312, 623
Robert, C. P., & Casella, G. 2018, Monte Carlo Statistical Methods (New York: Springer)
Samara, E., Laperre, B., Kieokaew, R., et al. 2022, ApJ, 927, 187
Silva, H. G., & Lopes, I. 2017, Ap&SS, 362, 44
Simoniello, R., Jain, K., Tripathy, S. C., et al. 2013, ApJ, 765, 100
Sivaraman, K. R., Gupta, S. S., & Howard, R. F. 1993, SoPh, 146, 27
Sokoloff, D. D., Shibalova, A. S., Obridko, V. N., & Pipin, V. V. 2020, MNRAS, 497, 4376
Stephens, M. A. 1974, JASA, 69, 730
Sturrock, P. A., Bertello, L., Fischbach, E., et al. 2013, APh, 42, 62
Temmer, M. 2021, LRSP, 18, 4
Temmer, M., Rybák, J., Bendík, P., et al. 2006, A&A, 447, 735
Temmer, M., Veronig, A., & Hanslmeier, A. 2002, A&A, 390, 707
Torrence, C., & Compo, G. P. 1998, BAMS, 79, 61
Ulrich, R. K. 2001, ApJ, 560, 466
Vecchio, A., & Carbone, V. 2009, A&A, 502, 981
Vecchio, A., Laurenza, M., Meduri, D., Carbone, V., & Storini, M. 2012, ApJ, 749, 27
Veronig, A. M., Jain, S., Podladchikova, T., Pötzi, W., & Clette, F. 2021, A&A, 652, A56
Wolf, R. 1851, AN, 32, 193
Wolf, R. 1861, MNRAS, 21, 77
Wolfer, A. 1902, PA, 10, 449
Young-Seon, J., Myong, K. J., & Olufemi, A. O. 2011, PatRe, 44, 2231
Zaqarashvili, T. 2018, ApJ, 856, 32
Zaqarashvili, T. V., Albekioni, M., Ballester, J. L., et al. 2021, SSRv, 217, 15
Zaqarashvili, T. V., Carbonell, M., Oliver, R., & Ballester, J. L. 2010a, ApJ, 709, 749
Zaqarashvili, T. V., Carbonell, M., Oliver, R., & Ballester, J. L. 2010b, ApJL, 724, L95
Zaqarashvili, T. V., Oliver, R., Ballester, J. L., & Shergelashvili, B. M. 2007, A&A, 470, 815
Zhang, C., Fanaee-T, H., & Thoresen, M. 2021, Data Min. Knowl. Disc., 35, 1760
Zolotova, N. V., & Ponyavin, D. I. 2015, Ge&Ae, 55, 902